



Cousins, J.R.L., Wilson, S.K., [Mottram, N.](#) , Wilkes, D. and Weegels, L. (2020) Transient flow-driven distortion of a nematic liquid crystal in channel flow with dissipative weak planar anchoring. *Physical Review E*, 102, 062703. (doi: [10.1103/PhysRevE.102.062703](https://doi.org/10.1103/PhysRevE.102.062703))

The material cannot be used for any other purpose without further permission of the publisher and is for private use only.

There may be differences between this version and the published version. You are advised to consult the publisher's version if you wish to cite from it.

<http://eprints.gla.ac.uk/226068/>

Deposited on 18 November 2020

Enlighten – Research publications by members of the University of  
Glasgow

<http://eprints.gla.ac.uk>

# Transient flow-driven distortion of a nematic liquid crystal in channel flow with dissipative weak planar anchoring

J. R. L. Cousins,<sup>1,\*</sup> S. K. Wilson,<sup>1,†</sup> N. J. Mottram,<sup>1,‡</sup> D. Wilkes,<sup>2</sup> and L. Weegels<sup>2,§</sup>

<sup>1</sup>*Department of Mathematics and Statistics, University of Strathclyde,  
Livingstone Tower, 26 Richmond Street, Glasgow G1 1XH, United Kingdom*

<sup>2</sup>*Merck KGaA, Frankfurter Str. 250, Darmstadt 64293, Germany*

(Dated: 22nd July 2020, revised 9th October 2020, accepted 9th November 2020)

## Abstract

Motivated by the One-Drop-Filling (ODF) method for the industrial manufacturing of Liquid Crystal Displays (LCDs), we analyse pressure-driven flow of a nematic in a channel with dissipative weak planar anchoring at the boundaries of the channel. We obtain quasi-steady asymptotic solutions for the director angle and the velocity in the limit of small Leslie angle, in which case the key parameters are the Ericksen number and the anchoring strength parameter. In the limit of large Ericksen number the solution for the director angle has narrow reorientational boundary layers and a narrow reorientational internal layer separated by two outer regions in which the director is aligned at the positive Leslie angle in the lower half of the channel and the negative Leslie angle in the upper half of the channel. On the other hand, in the limit of small Ericksen number the solution for the director angle is dominated by splay elastic effects with viscous effects appearing at first order. As the Ericksen number varies there is a continuous transition between these asymptotic behaviours and, in fact, the two asymptotic solutions capture the behaviour rather well for all values of the Ericksen number. The steady state value of the director angle at the boundaries and the timescale of the evolution towards this steady state value in the asymptotic limits of large and small Ericksen number are determined. In particular, using estimated parameter values for the ODF method it is found that the boundary director rotation timescale is substantially shorter than the timescale of the ODF method, suggesting that there is sufficient time for significant transient flow-driven distortion of the nematic molecules at the substrates from their required orientation to occur.

---

\* joseph.cousins@strath.ac.uk

† Author for correspondence; s.k.wilson@strath.ac.uk

‡ nigel.mottram@strath.ac.uk; Present Address: School of Mathematics and Statistics, University of Glasgow, University Place, Glasgow G12 8QQ, United Kingdom. Present Email: nigel.mottram@glasgow.ac.uk

§ leo.weegels@merckgroup.com

## I. INTRODUCTION

### A. Industrial Manufacturing of Liquid Crystal Displays

The industrial manufacturing of liquid crystal displays (LCDs) involves the creation of a thin layer of nematic liquid crystal (hereafter simply referred to as “nematic”) encapsulated between two solid substrates with the appropriate optical properties required for the correct functioning of the final device. The substrates typically consist of glass or plastic plates patterned with electrodes of indium tin oxide (ITO) and coated with thin alignment layers, whose purpose is to ensure that the nematic molecules have the required orientation at the substrates in the final device. The manufacturing of LCDs was previously carried out using the capillary-filling method [1], but, due to its superior scale and speed, this has now been almost entirely replaced by the One-Drop-Filling (ODF) method [1–3]. In capillary filling, the substrates are positioned parallel to each other with a typical gap size of around  $5\ \mu\text{m}$  [2]. The nematic is then introduced into this gap from one side of the device and allowed to fill the space between the substrates by capillary action, often aided by an applied pressure difference (an enhancement sometimes referred to as “vacuum filling”). Even with an applied pressure gradient, the nematic flow is still slow, and as such, capillary filling was a bottleneck in the manufacturing process, leading to manufacturing times of the order of a day [2, 4]. In ODF, the liquid crystal material in its nematic phase is dispensed onto the lower substrate in the form of droplets. These droplets are allowed to equilibrate and then the upper substrate is lowered towards the droplet-laden lower substrate, squeezing the droplets together to form the nematic layer. The introduction of the ODF method significantly improved manufacturing speeds so that manufacturing times were reduced from of the order of a day to of the order of an hour [2, 4], and are now even shorter than this. However, since ODF is significantly faster than capillary filling, it involves significantly higher nematic flow speeds, which may cause transient flow-driven distortion of the nematic molecules at the substrates from their required orientation. This may lead to permanent or semi-permanent flow-driven misalignment of the orientation of the molecules in the alignment layers, which may in turn degrade the optical properties of the final device. In particular, flow-driven misalignment of the orientation of the molecules in the alignment layers may be the cause of spurious optical effects known as “ODF mura” [5–7]. We have previously proposed a simple model for the formation of ODF mura due to coalescing droplets of a nematic [7] and have investigated how they might arise in the context of squeeze-film flow of a nematic [8]. In the present work we investigate a rather different fundamental aspect of the ODF method that may bring new insight into the formation of ODF mura, namely the possibility that significant transient flow-driven distortion of the nematic molecules at the substrates from their required orientation may occur during this method.

### B. The Alignment Layers

In industrial manufacturing of LCDs, the precision to which the required orientation of the nematic molecules at the substrates must be maintained is often extremely high. For instance, in vertically aligned nematic (VAN) devices, in which the required nematic orientation is close to  $90^\circ$ , deviations in the orientation as small as  $1^\circ$  can lead to unacceptably large changes of an order of magnitude in the LCD contrast ratio [9]. The alignment layers are

therefore crucial components of any LCD device. In particular, they are, in large part, responsible for determining its optical characteristics [10].

There are a number of methods for fabricating alignment layers. A widely-used method for creating a preferred orientation at the substrates is the Polymer Stabilised (PS) method. This method involves adding an ultraviolet (UV) curable monomer to the nematic and then applying a voltage difference across the device while exposing it to UV light in order to achieve the desired orientation at the polymer layers which form on both plates due to phase separation [11–13]. Another method for creating a preferred orientation at the substrates involves coating the plates with a layer of polyimide, and then mechanically rubbing these layers to create nano-grooves in their surfaces with which the nematic tends to align [10]. Other devices use photo-activated alignment in which the plates are coated in a polymer layer whose surface orientational properties are changed when they are exposed to polarised light [14]. All of the methods for creating an alignment layer rely on some form of adhesion between the molecules of the alignment layer and those of the nematic, which leads to an energetically preferred nematic orientation at the substrates. Depending on the alignment material used, the physical mechanism for this adhesion can be either mechanical or electrostatic [10]. The degree of preference for the preferred nematic orientation is related to the depth of the energy well in the interaction potential between the alignment layer and the nematic, and is measured by an appropriate anchoring strength.

### C. Dissipative Weak Anchoring

The aim of the present work is to investigate the possibility that significant transient flow-driven distortion of the nematic molecules at the substrates from their required orientation may occur during the manufacture of LCDs using the ODF method. To do this we use the standard continuum model for the flow of a nematic, namely Ericksen–Leslie theory [15–17]. Many other theories have been used to describe nematics, including Q-tensor theory [18], Berris–Edwards theory [19] and statistical theories [20], but Ericksen–Leslie theory is appropriate for the lengthscales present in device manufacturing. The Ericksen–Leslie equations describe the coupling of the average orientation of the nematic molecules, known as the director  $\mathbf{n}$ , the velocity  $\mathbf{u}$  and the pressure  $p$  through laws of conservation of mass, linear momentum and angular momentum [17]. In order to accurately model the behaviour of the director at the substrates, we consider both the interaction energy between molecules of the alignment layers and those of the nematic, and, importantly, the dissipation of energy that occurs close to the substrates. The competition between the preferred orientation and the orientation in the bulk of the nematic layer, which may be affected by forces due to flow or electric fields, means that the orientation of the director at the substrates may differ from the preferred orientation, albeit at an energy cost. Such a situation is usually referred to as “weak anchoring” [17, 21]. In particular, we use the so-called Rapini–Papoular anchoring energy [22], which models the preference of the director at the substrates to be at the preferred orientation. The Rapini–Papoular anchoring energy  $\omega$  [22] is of the form  $\omega = \gamma - A(\mathbf{n}_0 \cdot \mathbf{n})^2$ , where  $\mathbf{n}_0$  is the preferred orientation,  $\gamma$  is the isotropic interface tension, and  $A (\geq 0)$  is the anchoring strength. The Rapini–Papoular anchoring energy ensures that the surface energy is at a minimum when  $\mathbf{n}$  and  $\mathbf{n}_0$  are parallel. In particular, “planar anchoring” is when  $\mathbf{n}_0$  is parallel to the substrates, and “homeotropic anchoring” is when it is perpendicular to the substrates. The anchoring strength  $A$  (i.e. the binding energy per square metre) is a material

parameter which measures the strength of the adhesion between the alignment layer and the nematic. It has units of  $\text{Nm}^{-1}$  (i.e.  $\text{Jm}^{-2}$ ), and its values are typically found experimentally to lie in the range  $A = 10^{-5}$ – $10^{-3} \text{ Nm}^{-1}$  [23, 24]. The anchoring strength depends on both the nematic and the alignment material used [25]. Two important limits of weak anchoring are zero (or no) anchoring, corresponding to the limit  $A \rightarrow 0$ , in which the director has no preferred orientation at the substrates, and strong (or infinite) anchoring, corresponding to the limit  $A \rightarrow \infty$ , in which the director at the substrates is always aligned at the preferred orientation. While the anchoring energy describes the preference of the director for the preferred orientation, it does not capture the dynamical processes which take place close to the substrates. To include these we need to include surface dissipation, which models the dissipation of energy close to the substrates. We assume that the only such dissipation of energy occurs due to the rotation of the director. The surface dissipation is therefore proportional to  $\gamma_S (\partial \mathbf{n} / \partial t)^2$ , where  $\gamma_S (\geq 0)$  is the surface rotational viscosity. The surface rotational viscosity  $\gamma_S$  has units of  $\text{Pa s m}$ , and its values are typically found experimentally to lie in the range  $\gamma_S = 10^{-8}$ – $10^{-6} \text{ Pa s m}$  [26–28]. We use the term “dissipative weak anchoring” for the combined effects of weak anchoring and surface dissipation studied in the present work.

A dissipative weak anchoring condition has been used to study problems related to device switching, such as relaxation of director profiles and back flow (see, for example, [26, 29–35]), while Kléman and Píkin [36] formulated a dissipative weak anchoring condition in the context of Couette flow but only considered steady solutions. However, to the best of the authors’ knowledge, surprisingly little research has thus far been carried out on the influence of dissipative weak anchoring on the problem treated in the present work, namely channel flow. There has, however, been previous work on channel flow of a nematic without surface dissipation (for a summary of some of the early work on this problem see, for example, Quintans Carou et al. [37, 38] and the references therein). In particular, Quintans Carou et al. [37, 38] considered steady flow of a nematic in a slowly-varying channel in the special case of strong planar anchoring (i.e. in the special case in which the director at the boundaries of the channel is always aligned parallel to the boundaries). Specifically, Quintans Carou et al. [37, 38] used a combination of asymptotic and numerical methods to analyse the problem in the limit of small Leslie angle (defined in Section II C). Also relevant here is the more recent work on the transitions which occur in channel flow of a nematic with homeotropic anchoring observed experimentally by Sengupta et al. [39], and subsequently investigated theoretically by Anderson et al. [40] and Crespo et al. [41] for weak homeotropic anchoring, and numerically by Batista et al. [42] for weak homeotropic, planar and hybrid (i.e. homeotropic at one boundary and planar at the other boundary) anchoring.

## II. MODEL FORMULATION

### A. Governing Equations and Boundary Conditions

Consider unidirectional flow of a nematic with velocity in the  $x$ -direction within a two-dimensional channel with fixed boundaries located at  $z = 0$  and  $z = h$ , as shown in Figure 1, where  $(x, z)$  are Cartesian coordinates and  $t$  denotes time. The flow is driven by a prescribed constant pressure gradient in the  $x$ -direction, denoted by  $G = -dp/dx (> 0)$ , where  $p = p(x)$  is the fluid pressure, and we assume that the director remains in the  $(x, z)$  plane.

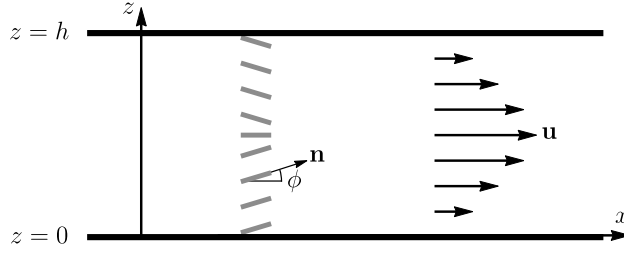


FIG. 1. Unidirectional pressure-driven flow of a nematic within a two-dimensional channel with fixed boundaries located at  $z = 0$  and  $z = h$ . The flow is driven by a prescribed constant pressure gradient in the  $x$ -direction,  $G = -dp/dx (> 0)$ , and is indicated by the black solid arrows. The director  $\mathbf{n}$  with director angle  $\phi$  is indicated by the grey lines. The Cartesian coordinates  $(x, z)$  are also indicated.

We therefore seek solutions for the director  $\mathbf{n} = \mathbf{n}(z, t)$  and the velocity  $\mathbf{u} = \mathbf{u}(z, t)$  in the channel in the forms

$$\mathbf{n} = (\cos(\phi(z, t)), 0, \sin(\phi(z, t))), \quad (1)$$

$$\mathbf{u} = (u(z, t), 0, 0), \quad (2)$$

where  $\phi = \phi(z, t)$  is the angle between the director and  $x$ -axis, hereafter referred to as the director angle, as shown in Figure 1. For this situation, the Ericksen–Leslie equations [15–17] for the director angle  $\phi$  and the velocity  $u$  are given by

$$\gamma_1 \frac{\partial \phi}{\partial t} = f(\phi) \frac{\partial^2 \phi}{\partial z^2} + \frac{1}{2} f'(\phi) \left( \frac{\partial \phi}{\partial z} \right)^2 - m(\phi) \frac{\partial u}{\partial z}, \quad (3)$$

$$\rho \frac{\partial u}{\partial t} = G + \frac{\partial}{\partial z} \left( g(\phi) \frac{\partial u}{\partial z} + m(\phi) \frac{\partial \phi}{\partial t} \right), \quad (4)$$

where the constants  $\rho$  and  $\gamma_1$  are the density and the bulk rotational viscosity, respectively. For a full derivation of the Ericksen–Leslie equations for rectilinear flow, see, for example, Appendix A of Crespo et al. [41]. The elasticity function  $f(\phi)$  and viscosity functions  $m(\phi)$  and  $g(\phi)$  appearing in (3) and (4) are defined by

$$f(\phi) = K_1 \cos^2 \phi + K_3 \sin^2 \phi, \quad (5)$$

$$m(\phi) = \alpha_3 \cos^2 \phi - \alpha_2 \sin^2 \phi, \quad (6)$$

$$g(\phi) = \frac{1}{2}(\alpha_4 + \alpha_3 + \alpha_6) \cos^2 \phi + \frac{1}{2}(\alpha_4 - \alpha_2 + \alpha_5) \sin^2 \phi + \alpha_1 \sin^2 \phi \cos^2 \phi, \quad (7)$$

respectively, where the constants  $K_1$  and  $K_3$  are the splay and bend elastic constants, and  $\alpha_1, \dots, \alpha_6$  are the Leslie viscosities (of which  $\alpha_4/2$  is the isotropic viscosity) [17]. The elasticity function  $f(\phi)$  is the effective elastic constant that the nematic exhibits in a simple shear flow with a fixed director angle  $\phi$ . The viscosity function  $m(\phi)$  describes the director-dependent coupling between the rotation of the director,  $\partial\phi/\partial t$ , and the shear rate,  $\partial u/\partial z$ . The viscosity function  $g(\phi)$  is the effective viscosity that the nematic exhibits in a simple shear flow with a fixed director angle  $\phi$ .

As described in Section IC, we take the boundary conditions for the director angle to be the so-called dissipative

weak anchoring conditions (see, for example, [26, 29–36]) given by

$$\gamma_S \frac{\partial \phi}{\partial t} = +f(\phi) \frac{\partial \phi}{\partial z} - A \sin 2\phi \quad \text{at } z = 0, \quad (8)$$

$$\gamma_S \frac{\partial \phi}{\partial t} = -f(\phi) \frac{\partial \phi}{\partial z} - A \sin 2\phi \quad \text{at } z = h, \quad (9)$$

where the constants  $\gamma_S (\geq 0)$  and  $A (\geq 0)$  are the surface rotational viscosity and the anchoring strength, respectively. For anchoring conditions of this form the preferred director orientation at the channel boundary is  $\phi \equiv p\pi$ , where  $p$  is an integer. The present analysis is relevant to devices with planar anchoring for which the preferred director orientations at the substrates are parallel, such as In-Plane Switching (IPS) devices [43]. While the present analysis is not directly relevant to devices with homeotropic anchoring, such as VAN devices [12], or to devices in which the director does not remain in the  $(x, z)$  plane, such as Twisted Nematic (TN) or Super-Twisted Nematic (STN) devices [44], we anticipate that many of the qualitative features of the present results will also occur in these devices.

For the velocity we impose standard no-slip boundary conditions given by

$$u = 0 \quad \text{at } z = 0, \quad (10)$$

$$u = 0 \quad \text{at } z = h. \quad (11)$$

Appropriate initial conditions on  $\phi$  and  $u$  will be described in Section IID.

## B. Non-Dimensionalisation

The governing equations (3) and (4) with (5), (6) and (7) subject to (8)–(11) are non-dimensionalised according to

$$t = \tau \tilde{t}, \quad z = h \tilde{z}, \quad u = \frac{Gh^2}{\alpha_4} \tilde{u}, \quad f = K_1 \tilde{f}, \quad m = \alpha_4 \tilde{m}, \quad g = \alpha_4 \tilde{g}, \quad (12)$$

$$K_3 = K_1 \tilde{K}_3, \quad \alpha_i = \alpha_4 \tilde{\alpha}_i \quad \text{for } i = 1, \dots, 6, \quad \gamma_i = \alpha_4 \tilde{\gamma}_i \quad \text{for } i = 1, 2,$$

where  $\tau$  is an appropriate timescale, which will be discussed in detail in Section IID, and non-dimensional variables are denoted by a superimposed tilde ( $\tilde{\phantom{x}}$ ). Note that the velocity is non-dimensionalised using the characteristic velocity of pressure-driven channel flow of a Newtonian fluid, which depends on  $G$ ,  $h$  and  $\alpha_4$ , the elastic function  $f$  and the bend elastic constant  $K_3$  are non-dimensionalised with the splay elastic constant  $K_1$ , while the viscosity functions  $m$  and  $g$ , the Leslie viscosities  $\alpha_i$  for  $i = 1, \dots, 6$ , the bulk rotational viscosity  $\gamma_1$ , and the torsional viscosity  $\gamma_2$  are all non-dimensionalised with  $\alpha_4$ .

The non-dimensional Ericksen–Leslie equations (3) and (4) are given by

$$\frac{\gamma_1 h^2}{K_1 \tau} \frac{\partial \phi}{\partial \tilde{t}} = \tilde{f}(\phi) \frac{\partial^2 \phi}{\partial \tilde{z}^2} + \frac{1}{2} \tilde{f}'(\phi) \left( \frac{\partial \phi}{\partial \tilde{z}} \right)^2 - \text{Er} \tilde{m}(\phi) \frac{\partial \tilde{u}}{\partial \tilde{z}}, \quad (13)$$

$$\text{Re} \frac{\alpha_4}{Gh\tau} \frac{\partial \tilde{u}}{\partial \tilde{t}} = 1 + \frac{\partial}{\partial \tilde{z}} \left( \tilde{g}(\phi) \frac{\partial \tilde{u}}{\partial \tilde{z}} + \frac{\alpha_4}{Gh\tau} \tilde{m}(\phi) \frac{\partial \phi}{\partial \tilde{t}} \right), \quad (14)$$

where the non-dimensional elasticity and viscosity functions (5)–(7) are given by

$$\tilde{f}(\phi) = \cos^2 \phi + \tilde{K}_3 \sin^2 \phi, \quad (15)$$

$$\tilde{m}(\phi) = \tilde{\alpha}_3 \cos^2 \phi - \tilde{\alpha}_2 \sin^2 \phi, \quad (16)$$

$$\tilde{g}(\phi) = \frac{1}{2}(1 + \tilde{\alpha}_3 + \tilde{\alpha}_6) \cos^2 \phi + \frac{1}{2}(1 - \tilde{\alpha}_2 + \tilde{\alpha}_5) \sin^2 \phi + \tilde{\alpha}_1 \sin^2 \phi \cos^2 \phi, \quad (17)$$

the non-dimensional dissipative weak anchoring conditions (8) and (9) are

$$\frac{\gamma_S h}{K_1 \tau} \frac{\partial \phi}{\partial \tilde{t}} = + \tilde{f}(\phi) \frac{\partial \phi}{\partial \tilde{z}} - \mathcal{A} \sin 2\phi \quad \text{at } \tilde{z} = 0, \quad (18)$$

$$\frac{\gamma_S h}{K_1 \tau} \frac{\partial \phi}{\partial \tilde{t}} = - \tilde{f}(\phi) \frac{\partial \phi}{\partial \tilde{z}} - \mathcal{A} \sin 2\phi \quad \text{at } \tilde{z} = 1, \quad (19)$$

and the non-dimensional no-slip conditions (10) and (11) are

$$\tilde{u} = 0 \quad \text{at } \tilde{z} = 0, \quad (20)$$

$$\tilde{u} = 0 \quad \text{at } \tilde{z} = 1. \quad (21)$$

Equations (13)–(21) involve three key non-dimensional groups, namely the Ericksen number  $\text{Er}$  defined by

$$\text{Er} = \frac{Gh^3}{K_1}, \quad (22)$$

the Reynolds number  $\text{Re}$  defined by

$$\text{Re} = \frac{\rho Gh^3}{\alpha_4^2}, \quad (23)$$

and the anchoring strength parameter  $\mathcal{A}$  defined by

$$\mathcal{A} = \frac{Ah}{K_1}. \quad (24)$$

The Ericksen number  $\text{Er}$  is a non-dimensional measure of the relative strength of viscous effects and splay elastic effects. The limit of zero Ericksen number ( $\text{Er} \rightarrow 0$ ) corresponds to a regime in which there are no viscous effects, while the limit of infinite Ericksen number ( $\text{Er} \rightarrow \infty$ ) corresponds to a regime in which there are no elastic effects. The familiar Reynolds number  $\text{Re}$  is a non-dimensional measure of the relative strength of inertial effects and viscous effects. The limit of zero Reynolds number ( $\text{Re} \rightarrow 0$ ) corresponds to a regime in which there are no inertial effects (i.e. Stokes flow), while the limit of infinite Reynolds number ( $\text{Re} \rightarrow \infty$ ) corresponds to a regime in which there are no viscous effects (i.e. inviscid flow). The anchoring strength parameter  $\mathcal{A}$  is a non-dimensional measure of the relative strength of anchoring and splay elastic effects at the boundaries. As described in Section IC, the limit of zero anchoring strength parameter ( $\mathcal{A} \rightarrow 0$ ) corresponds to a regime in which there is zero anchoring at the boundaries, while the limit of infinite anchoring strength parameter ( $\mathcal{A} \rightarrow \infty$ ) corresponds to a regime in which there is strong anchoring at the boundaries.

Solving the governing equations and boundary conditions (13)–(21) must, in general, be done numerically. However, in the present work we follow an approach similar to that of Quintans Carou et al. [37, 38] and use a combination of asymptotic and numerical methods to analyse the problem in the limit of small Leslie angle.



### C. The Leslie Angle

When the director field is static and uniformly orientated, i.e. when  $\phi = \text{constant}$ , from (13) a uniform shear flow leads to the condition  $\tilde{m}(\phi) = 0$ . For flow-aligning nematics, i.e. for nematics whose viscosities satisfy  $\tilde{\alpha}_3/\tilde{\alpha}_2 \geq 0$ , the director angle then takes the value  $\phi = p\pi \pm \phi_L$ , where  $\phi_L$  ( $0 \leq \phi_L \leq \pi/2$ ) is the Leslie angle (sometimes also called the flow alignment angle) [17], and is defined by

$$\phi_L = \tan^{-1} \sqrt{\frac{\tilde{\alpha}_3}{\tilde{\alpha}_2}}. \quad (25)$$

A stability analysis of the system shows that in a region of positive shear rate ( $\partial u/\partial z > 0$ ) or negative shear rate ( $\partial u/\partial z < 0$ ) the director remains in the  $(x, z)$  plane and the director angle rotates towards the ‘‘positive’’ Leslie angle  $\phi = p\pi + \phi_L$  or the ‘‘negative’’ Leslie angle  $\phi = p\pi - \phi_L$ , respectively, [17, 45, 46]. In particular, for a flow-aligning nematic the director angle approaches  $\phi = p\pi \pm \phi_L$  when viscous effects dominate splay elastic effects (i.e. when  $Er \gg 1$ ), in which case reorientational boundary and/or internal layers may occur between the uniformly orientated bulk and/or the orientation dictated by the boundaries [17, 37–42]. On the other hand, for non-flow-aligning nematics, i.e. for nematics whose viscosities satisfy  $\tilde{\alpha}_3/\tilde{\alpha}_2 < 0$ , the Leslie angle does not exist and the director exhibits unsteady behaviour known as tumbling [17, 47].

In the present work we will consider only flow-aligning nematics and introduce a non-dimensional viscosity ratio denoted by  $\epsilon$  ( $\geq 0$ ) and defined by

$$\epsilon = \sqrt{\frac{\tilde{\alpha}_3}{\tilde{\alpha}_2}}, \quad (26)$$

so that the Leslie angle defined by (25) can be written in terms of  $\epsilon$  as  $\phi_L = \tan^{-1} \epsilon$ . The viscosity ratio  $\epsilon$  can also be expressed in terms of the more commonly measured bulk rotational viscosity  $\tilde{\gamma}_1$  and torsional viscosity  $\tilde{\gamma}_2$  [17] as

$$\epsilon = \sqrt{\frac{\tilde{\gamma}_1 + \tilde{\gamma}_2}{\tilde{\gamma}_2 - \tilde{\gamma}_1}}. \quad (27)$$

For nematic materials that are commonly used in industrial manufacturing of LCDs, typically  $\epsilon$  is small. For example,  $\epsilon \simeq 0.210$  for 4-Cyano-4'-pentylbiphenyl (5CB) [17],  $\epsilon \simeq 0.143$  for 4-Cyano-4'-heptylbiphenyl (7CB) [48], and  $\epsilon \simeq 0.001$  for 4-Cyano-4'-octyloxybiphenyl (8OCB) [49]. In fact, most modern LCDs use mixtures of nematics with physical properties similar to E7, which contains 51% 5CB, 25% 7CB, 16% 8OCB and 8% of other similar biphenyl compounds [50], and so typically  $\epsilon$  is also small for these mixtures. In Section III we will exploit the smallness of  $\epsilon$  to seek asymptotic solutions in the limit  $\epsilon \rightarrow 0$ .

For future reference, we note that the non-dimensional viscosity functions  $\tilde{m}(\phi)$  and  $\tilde{g}(\phi)$  given by (16) and (17) can be written without explicitly mentioning  $\tilde{\alpha}_3 = \epsilon^2 \tilde{\alpha}_2$  as

$$\tilde{m}(\phi) = \tilde{\alpha}_2 (-\sin^2 \phi + \epsilon^2 \cos^2 \phi), \quad (28)$$

$$\tilde{g}(\phi) = \frac{1}{2} (1 + \epsilon^2 \tilde{\alpha}_2 + \tilde{\alpha}_6) \cos^2 \phi + \frac{1}{2} (1 - \tilde{\alpha}_2 + \tilde{\alpha}_5) \sin^2 \phi + \tilde{\alpha}_1 \sin^2 \phi \cos^2 \phi. \quad (29)$$

## D. Timescales

We now discuss four timescales occurring in (13)–(21), namely

$$\tau_1 = \frac{\gamma_1 h^2}{K_1}, \quad \tau_2 = \frac{\rho h^2}{\alpha_4}, \quad \tau_3 = \frac{\alpha_2}{Gh}, \quad \tau_4 = \frac{\gamma_S h}{K_1}, \quad (30)$$

over which different physical effects occur.

Using the definitions (28) and (30) in (13), (14), (18) and (19) yields the governing equations

$$\frac{\tau_1}{\tau} \frac{\partial \phi}{\partial \tilde{t}} = \tilde{f}(\phi) \frac{\partial^2 \phi}{\partial \tilde{z}^2} + \frac{1}{2} \tilde{f}'(\phi) \left( \frac{\partial \phi}{\partial \tilde{z}} \right)^2 - \tilde{\alpha}_2 \text{Er} (\epsilon^2 \cos^2 \phi - \sin^2 \phi) \frac{\partial \tilde{u}}{\partial \tilde{z}}, \quad (31)$$

$$\frac{\tau_2}{\tau} \frac{\partial \tilde{u}}{\partial \tilde{t}} = 1 + \frac{\partial}{\partial \tilde{z}} \left[ \tilde{g}(\phi) \frac{\partial \tilde{u}}{\partial \tilde{z}} + \frac{\tau_3}{\tau} (\epsilon^2 \cos^2 \phi - \sin^2 \phi) \frac{\partial \phi}{\partial \tilde{t}} \right], \quad (32)$$

and the dissipative weak anchoring conditions

$$\frac{\tau_4}{\tau} \frac{\partial \phi}{\partial \tilde{t}} = + \tilde{f}(\phi) \frac{\partial \phi}{\partial \tilde{z}} - \mathcal{A} \sin 2\phi \quad \text{at } \tilde{z} = 0, \quad (33)$$

$$\frac{\tau_4}{\tau} \frac{\partial \phi}{\partial \tilde{t}} = - \tilde{f}(\phi) \frac{\partial \phi}{\partial \tilde{z}} - \mathcal{A} \sin 2\phi \quad \text{at } \tilde{z} = 1. \quad (34)$$

The *bulk director rotation timescale*  $\tau_1$  appears in the angular momentum equation (31) and is the timescale of rotation of the director within the bulk of the channel induced by the splay elastic reorientation towards a uniform director. The *fluid inertia timescale*  $\tau_2$  appears in the linear momentum equation (32) and is the familiar inertial timescale for a Newtonian fluid. The *director-flow coupling timescale*  $\tau_3$  also appears in the linear momentum equation (32) and is the timescale on which changes in the velocity affect the director orientation and vice versa. The *boundary director rotation timescale*  $\tau_4$  appears in the dissipative weak anchoring conditions (33) and (34) and is the timescale of rotation of the director at the boundaries of the channel driven by splay elastic effects. In contrast to the bulk rotation timescale  $\tau_1$ , the boundary director rotation timescale  $\tau_4$  depends on the surface rotational viscosity  $\gamma_S$  rather than the bulk rotational viscosity  $\gamma_1$ . The timescales  $\tau_1$  and  $\tau_4$  depend on splay elastic reorientation, for a discussion of the timescales depending on twist elastic reorientation (i.e. those depending on  $K_2$ ), the reader is referred to the work of Rey [29].

In order to obtain order-of-magnitude estimates of the timescales  $\tau_1$ ,  $\tau_2$ ,  $\tau_3$  and  $\tau_4$  in the ODF method we used estimated parameter values for a typical nematic mixture used in industrial manufacturing of LCDs, namely a nematic density  $\rho = 10^3 \text{ kg m}^{-3}$  [17], surface rotational viscosity  $\gamma_S = 10^{-8} \text{--} 10^{-6} \text{ Pa s m}$  [26, 27], Leslie viscosities  $\alpha_2 = 10^{-2} \text{ Pa s}$  and  $\alpha_4 = 10^{-1} \text{ Pa s}$  [17, 49], bulk rotational viscosity  $\gamma_1 = 10^{-2} \text{ Pa s}$  [17], viscosity ratio  $\epsilon = 10^{-1}$ , splay elastic constant  $K_1 = 10^{-11} \text{ N}$  [17], and cell gap  $h = 10^{-6} \text{ m}$  [7]. To estimate the timescale  $\tau_3$  we require an estimate of the pressure gradient  $G$ . The flow of the nematic in the ODF method is driven by the squeezing together of the substrates, and so the pressure gradient can be estimated by using the pressure gradient of squeeze-film flow of a Newtonian fluid, namely  $G = \alpha_4 L w_p / h^3$ , where  $L$  is the horizontal length scale of the flow and  $w_p$  is the speed at which the substrates are squeezed together [51]. The timescale of the ODF method, denoted by  $\tau_{\text{ODF}}$ , is the timescale over which the substrates are squeezed together. We take the horizontal length scale to be the typical diameter of a nematic droplet used in the ODF method, namely  $L = 10^{-2} \text{ m}$  [7, 8], the typical ODF timescale  $\tau_{\text{ODF}} = 10^{-1} \text{ s}$  [7], and the speed at which the substrates are squeezed together to be  $w_p = 10^{-3} \text{ m s}^{-1}$  [7, 8], which yields an estimate of the pressure gradient in the ODF method of  $G = 10^{12} \text{ Pa m}^{-1}$ .

Timescale	Definition	Physical Meaning	Value
$\tau_1$	$\frac{\gamma_1 h^2}{K_1}$	bulk director rotation	$10^{-3}$ s
$\tau_2$	$\frac{\rho h^2}{\alpha_4}$	fluid inertia	$10^{-8}$ s
$\tau_3$	$\frac{\alpha_2}{Gh}$	director-flow coupling	$10^{-8}$ s
$\tau_4$	$\frac{\gamma_S h}{K_1}$	boundary director rotation	$10^{-3}$ – $10^{-1}$ s

TABLE I. Order-of-magnitude estimates of the timescales  $\tau_1$ ,  $\tau_2$ ,  $\tau_3$  and  $\tau_4$  in the ODF method using the estimated parameter values given in the text.

Table I shows order-of-magnitude estimates of the timescales  $\tau_1$ ,  $\tau_2$ ,  $\tau_3$  and  $\tau_4$  in the ODF method using the estimated parameter values given above. In particular, Table I shows that the fluid inertia timescale and director flow coupling timescale,  $\tau_2$  and  $\tau_3$ , are much shorter than the two director rotation timescales,  $\tau_1$  and  $\tau_4$ , and so these effects can safely be treated as instantaneous on the timescale of the ODF method, and henceforth we set  $\tau_2 = 0$  and  $\tau_3 = 0$ . The two director rotation timescales are comparable when  $\gamma_S = 10^{-8}$  Pa s m, suggesting that the regime in which  $\tau = \tau_1 \simeq \tau_4$  is worthy of study, but since  $\tau_1$  is 100 times shorter than  $\tau_4$  when  $\gamma_S = 10^{-6}$  Pa s m, in the present work we also set  $\tau_1 = 0$ . Since all of the timescales except the boundary director rotation timescale  $\tau_4$  have been set to zero, we can now, without loss of generality, set  $\tau = \tau_4$ , so that the governing equations (31) and (32) become

$$\tilde{f}(\phi) \frac{\partial^2 \phi}{\partial \tilde{z}^2} + \frac{1}{2} \tilde{f}'(\phi) \left( \frac{\partial \phi}{\partial \tilde{z}} \right)^2 = \tilde{\alpha}_2 \text{Er} (\epsilon^2 \cos^2 \phi - \sin^2 \phi) \frac{\partial \tilde{u}}{\partial \tilde{z}}, \quad (35)$$

$$0 = 1 + \frac{\partial}{\partial \tilde{z}} \left( g(\phi) \frac{\partial \tilde{u}}{\partial \tilde{z}} \right), \quad (36)$$

subject to the dissipative weak anchoring conditions (18) and (19),

$$\frac{\partial \phi}{\partial \tilde{t}} = + \tilde{f}(\phi) \frac{\partial \phi}{\partial \tilde{z}} - \mathcal{A} \sin 2\phi \quad \text{at} \quad \tilde{z} = 0, \quad (37)$$

$$\frac{\partial \phi}{\partial \tilde{t}} = - \tilde{f}(\phi) \frac{\partial \phi}{\partial \tilde{z}} - \mathcal{A} \sin 2\phi \quad \text{at} \quad \tilde{z} = 1, \quad (38)$$

and the no-slip conditions (20) and (21), where the tilde ( $\tilde{\phantom{x}}$ ) notation on non-dimensional variables has been dropped for clarity.

Given that the time derivatives have been removed from the governing equations (35) and (36), leaving only time derivatives of the director angle in the dissipative weak anchoring conditions (37) and (38), we no longer require initial conditions on the director angle and the velocity (i.e.  $\phi(z, 0)$  and  $u(z, 0)$ ) within the bulk of the channel. Instead we only require initial conditions on the director angle at the boundaries (i.e.  $\phi(0, 0)$  and  $\phi(1, 0)$ ). Specifically, we impose initial conditions on the director angle at the boundaries in the form

$$\phi = + \phi_L \theta \quad \text{at} \quad z = 0 \quad \text{and} \quad t = 0, \quad (39)$$

$$\phi = - \phi_L \theta \quad \text{at} \quad z = 1 \quad \text{and} \quad t = 0, \quad (40)$$

where  $\theta (\geq 0)$  is the magnitude of the initial director angle at the boundaries scaled with  $\phi_L$ .

At this point it is useful to consider typical values of the important non-dimensional groups  $\text{Er}$  and  $\mathcal{A}$  in the ODF method.

Using the values in Table I, the Ericksen number is found to be  $\text{Er} = 10^5$ , indicating that the flow is usually dominated by viscous effects. However, this large value is slightly misleading because, as we will show in Section III, the effective Ericksen number, denoted by  $\bar{\text{Er}}$ , takes the somewhat smaller value  $\bar{\text{Er}} = 1.7 \times 10^2$  and so, for completeness, we will consider all values of  $\bar{\text{Er}}$  in what follows.

As mentioned in Section IC, anchoring strengths are typically found experimentally to lie in the range of  $A = 10^{-5}$ – $10^{-3} \text{ N m}^{-1}$  [26, 27], and so, using (24) and the values in Table I, this corresponds to values of the anchoring strength parameter in the range  $\mathcal{A} = 1$ – $10^2$ .

### III. ASYMPTOTIC SOLUTIONS IN THE LIMIT OF SMALL LESLIE ANGLE

As described in Section II C, typically the viscosity ratio  $\epsilon$  for commonly used nematics and mixtures of nematics is small, and so henceforth we obtain asymptotic solutions in the limit  $\epsilon \rightarrow 0$ . In particular, in this limit the Leslie angle  $\phi_L = \tan^{-1} \epsilon \sim \epsilon \ll 1$  is small.

In the limit  $\epsilon \rightarrow 0$  we seek asymptotic solutions for  $\phi$  and  $u$  in powers of  $\epsilon$  in the forms

$$\phi(z, t) = \phi_0(z, t) + \epsilon \phi_1(z, t) + \epsilon^2 \phi_2(z, t) + O(\epsilon^3), \quad (41)$$

$$u(z, t) = u_0(z, t) + \epsilon u_1(z, t) + \epsilon^2 u_2(z, t) + O(\epsilon^3). \quad (42)$$

Substituting the expansions (41) and (42) into the angular momentum equation (35), the linear momentum equation (36), the dissipative weak anchoring conditions (37) and (38), the initial conditions (39) and (40), and the no-slip conditions (20) and (21), and defining an appropriately rescaled *effective Ericksen number*  $\bar{\text{Er}}$  [37, 38] (hereafter simply referred to as the Ericksen number) given by

$$\bar{\text{Er}} = -\frac{\epsilon \alpha_2}{1 + \alpha_6} \text{Er}, \quad (43)$$

yields the leading-order equations

$$0 = \sin^2 \phi_0 \frac{\partial u_0}{\partial z}, \quad (44)$$

$$0 = 1 + \frac{\partial}{\partial z} \left( g(\phi_0) \frac{\partial u_0}{\partial z} \right), \quad (45)$$

subject to the leading-order dissipative weak anchoring conditions

$$\frac{\partial \phi_0}{\partial t} = +f(\phi_0) \frac{\partial \phi_0}{\partial z} - 2\mathcal{A}\phi_0 \quad \text{at } z = 0, \quad (46)$$

$$\frac{\partial \phi_0}{\partial t} = -f(\phi_0) \frac{\partial \phi_0}{\partial z} - 2\mathcal{A}\phi_0 \quad \text{at } z = 1. \quad (47)$$

(Note that the definition of  $\bar{\text{Er}}$  given in (43) incorporates the  $O(1)$  factor of  $-\alpha_2/(1 + \alpha_6)$  in order to simplify some of the subsequent expressions.)

The leading-order director angle is obtained by solving (44) and (45) subject to the (46) and (47) to yield the trivial solution  $\phi_0 \equiv 0$ , i.e. the leading-order director angle is planar throughout the channel, and so at leading order the functions  $f(\phi)$  and  $g(\phi)$  appearing in (35)–(38) are given by  $f(\phi) = 1$  and  $g(\phi) = (1 + \alpha_6)/2$ .

The leading-order velocity is determined by integrating (45) with  $\phi_0 \equiv 0$  subject to the no-slip conditions (20) and (21) to obtain the classical Poiseuille flow profile

$$u_0 = \frac{z(1-z)}{1 + \alpha_6}. \quad (48)$$

The first-order angular momentum equation is identically satisfied, and the first-order linear momentum equation has the trivial solution  $u_1 \equiv 0$ .

The first-order director angle then satisfies the second-order angular momentum equation

$$\frac{\partial^2 \phi_1}{\partial z^2} = \bar{\text{Er}}(2z-1)(1-\phi_1^2), \quad (49)$$

subject to the first-order dissipative weak anchoring conditions

$$\frac{\partial \phi_1}{\partial t} = + \frac{\partial \phi_1}{\partial z} - 2\mathcal{A}\phi_1 \quad \text{at } z = 0, \quad (50)$$

$$\frac{\partial \phi_1}{\partial t} = - \frac{\partial \phi_1}{\partial z} - 2\mathcal{A}\phi_1 \quad \text{at } z = 1, \quad (51)$$

and the first-order initial conditions

$$\phi_1 = +\theta \quad \text{at } z = 0 \quad \text{and } t = 0, \quad (52)$$

$$\phi_1 = -\theta \quad \text{at } z = 1 \quad \text{and } t = 0. \quad (53)$$

The second-order velocity satisfies the second-order linear momentum equation

$$0 = \frac{\partial}{\partial z} \left[ \alpha_2 \frac{\partial u_0}{\partial z} + (2\alpha_1 - \alpha_2 + \alpha_5 - \alpha_6) \phi_1^2 \frac{\partial u_0}{\partial z} + (1 + \alpha_6) \frac{\partial u_2}{\partial z} \right], \quad (54)$$

which can be integrated subject to the no-slip conditions (20) and (21) to obtain

$$u_2 = \frac{2\alpha_1 - \alpha_2 + \alpha_5 - \alpha_6}{(1 + \alpha_6)^2} \left[ \int_0^z (2Z-1)\phi_1^2 dZ - z \int_0^1 (2z-1)\phi_1^2 dz \right] + \frac{\alpha_2}{(1 + \alpha_6)^2} z(z-1). \quad (55)$$

In the remainder of the present work we shall discuss the quasi-steady solutions for the first-order director angle  $\phi_1$  (hereafter simply referred to as “the director angle”) of (49) (hereafter simply referred to as “the director angle equation”) subject to the dissipative weak anchoring conditions (50) and (51), and the initial conditions (52) and (53). In particular, we will obtain asymptotic solutions in the limit of large Ericksen number  $\bar{\text{Er}} \rightarrow \infty$  in Section IV and in the limit of small Ericksen number  $\bar{\text{Er}} \rightarrow 0$  in Section V, as well as numerical solutions for general values of the Ericksen number in Section VI. Since we are particularly interested in the transient flow-driven distortion of the director from its required orientation at the boundaries of the channel, we write  $\Phi(t) = \phi_1(0, t)$  for the director angle at  $z = 0$  (hereafter simply referred to as “the director angle at the boundaries”), and note that since  $\phi_1$  is symmetric about  $z = 1/2$ , the director angle at  $z = 1$  is given by  $\phi_1(1, t) = -\Phi(t)$ . As we shall show, in the limit  $t \rightarrow \infty$  the director angle approaches a steady state solution which we denote by  $\phi_1 = \phi_{1\text{SS}}(z)$  and  $\Phi = \Phi_{\text{SS}}$ , i.e.  $\phi_1 \rightarrow \phi_{1\text{SS}}$  and  $\Phi \rightarrow \Phi_{\text{SS}}$  as  $t \rightarrow \infty$ . Once the director angle  $\phi_1$  has been determined, the second-order velocity  $u_2$  can be calculated using (55), but we do not undertake this calculation in the present work.

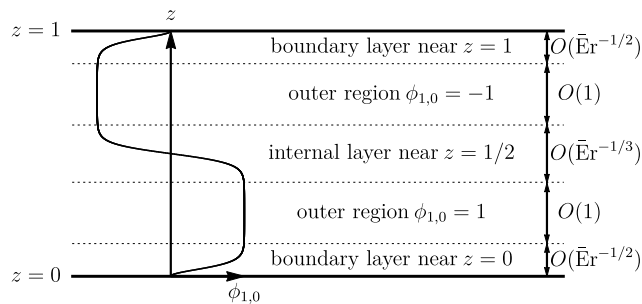


FIG. 2. The structure of the leading-order director angle  $\phi_{1,0}$  in the limit of large Ericksen number,  $\bar{\text{Er}} \rightarrow \infty$ .

#### IV. ASYMPTOTIC SOLUTION IN THE LIMIT OF LARGE ERICKSEN NUMBER

In the limit of large Ericksen number  $\bar{\text{Er}} \rightarrow \infty$  the solution for the director angle  $\phi_1$  has narrow reorientational boundary layers near  $z = 0$  and  $z = 1$  and a narrow reorientational internal layer near  $z = 1/2$  separated by two outer regions, as shown in Figure 2.

##### A. Outer Solution

The outer solution valid in the outer regions away from the boundary and internal layers can be obtained by seeking an asymptotic solution for  $\phi_1$  in powers of  $\bar{\text{Er}}^{-1}$  when  $\epsilon \ll \bar{\text{Er}}^{-1} \ll 1$  in the form  $\phi_1 = \phi_{1,0} + O(\bar{\text{Er}}^{-1})$ , where  $\phi_{1,0}$  denotes the term that is first order in  $\epsilon$  and leading order in  $\bar{\text{Er}}^{-1}$ . Substituting this expansion into the director angle equation (49) yields the simple solution  $\phi_{1,0} = \pm 1$ , which corresponds to the director angle being equal to either the positive or the negative Leslie angle at leading order. The leading-order velocity  $u_0$  given by (48) satisfies  $\partial u_0 / \partial z > 0$  for  $0 < z < 1/2$  and  $\partial u_0 / \partial z < 0$  for  $1/2 < z < 1$ , and so, as described in Section II C, the appropriate uniformly orientated leading-order outer solution is  $\phi_{1,0} = 1$  for  $0 < z < 1/2$  and  $\phi_{1,0} = -1$  for  $1/2 < z < 1$ , as shown in Figure 2.

##### B. Inner Solutions in the Boundary Layers

Inspection of (49) suggests that the boundary layer near  $z = 0$  is of width  $O(\bar{\text{Er}}^{-1/2}) \ll 1$  in which the director angle adjusts from its uniform value in the outer region to its value at the boundary, and so we introduce an appropriately rescaled inner coordinate  $Z$  defined by  $z = \bar{\text{Er}}^{-1/2} Z$  to yield

$$\frac{\partial^2 \phi_1}{\partial Z^2} = \left( 2\bar{\text{Er}}^{-1/2} Z - 1 \right) (1 - \phi_1^2). \quad (56)$$

Seeking an asymptotic solution of (56) in the form  $\phi_1 = \phi_{1,0} + O(\bar{\text{Er}}^{-1/2})$  yields the leading-order equation

$$\frac{\partial^2 \phi_{1,0}}{\partial Z^2} = \phi_{1,0}^2 - 1. \quad (57)$$

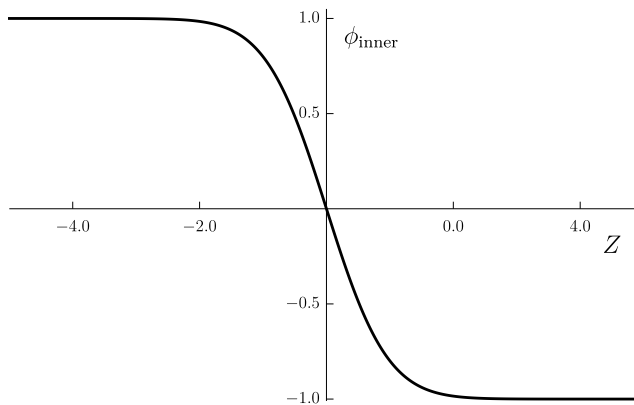


FIG. 3. The leading-order director angle in the internal layer  $\phi_{\text{inner}}$  obtained by solving (60) numerically using the matching conditions  $\phi_{\text{inner}} \rightarrow -1$  as  $Z \rightarrow \infty$  and  $\phi_{\text{inner}} \rightarrow 1$  as  $Z \rightarrow -\infty$  plotted as a function of the inner variable  $Z$ .

The appropriate exact solution of (57) subject to the matching conditions  $\phi_{1,0} \rightarrow 1$  and  $\partial\phi_{1,0}/\partial Z \rightarrow 0$  as  $Z \rightarrow \infty$  is

$$\phi_{1,0} = 3 \tanh^2 \left( \frac{Z}{\sqrt{2}} + \tanh^{-1} \sqrt{\frac{2 + \Phi_0}{3}} \right) - 2, \quad (58)$$

where  $\Phi_0(t) = \phi_{1,0}(0, t)$  is the leading-order director angle at the boundaries. Note that setting  $\Phi_0 \equiv 0$  in (58) recovers the steady solution obtained by Quintans Carou et al. [37, 38] in the limit of strong planar anchoring,  $\mathcal{A} \rightarrow \infty$ . However, in the present problem  $\Phi_0$  is, of course, not constant, and the singular ordinary differential equation for the evolution of  $\Phi_0$  can be obtained by substituting  $\phi_{1,0}$  given by (58) into the dissipative weak anchoring condition (50) to yield

$$\bar{\text{Er}}^{-1/2} \frac{d\Phi_0}{dt} = \sqrt{\frac{2}{3}} (1 - \Phi_0) \sqrt{2 + \Phi_0} - 2k\Phi_0, \quad \text{where } k = \frac{\mathcal{A}}{\bar{\text{Er}}^{1/2}} (\geq 0). \quad (59)$$

In Section IV E we will consider the solution to (59) subject to the initial condition  $\Phi_0(0) = \theta$ . The corresponding inner solution valid in the boundary layer near  $z = 1$  follows immediately from the symmetry of  $\phi_1$  about  $z = 1/2$  mentioned earlier.

### C. Inner Solution in the Internal Layer

Inspection of (49) also suggests that the internal layer near  $z = 1/2$  is of width  $O(\bar{\text{Er}}^{-1/3}) \ll 1$  (i.e. much wider than the boundary layers but still much narrower than the channel) in which the director angle adjusts between its uniform values in the outer regions, and so we introduce an appropriately rescaled inner coordinate  $Z$  defined by  $z = 1/2 + \bar{\text{Er}}^{-1/3}Z$ . Seeking an asymptotic solution in the form  $\phi_1 = \phi_{1,0} + O(\bar{\text{Er}}^{-1/3})$  yields the leading-order equation

$$\frac{\partial^2 \phi_{1,0}}{\partial Z^2} = 2Z(1 - \phi_{1,0}^2) \quad (60)$$

subject to the matching conditions  $\phi_{1,0} \rightarrow -1$  as  $Z \rightarrow \infty$  and  $\phi_{1,0} \rightarrow 1$  as  $Z \rightarrow -\infty$ . Equation (60) cannot be solved analytically, but, since it contains no parameters, it only needs to be solved once numerically. This numerical solution is denoted by  $\phi_{\text{inner}}(Z) = \phi_{1,0}(Z)$  and is plotted as a function of  $Z$  in Figure 3.

## D. Composite Solution

Combining the inner and outer solutions for  $\phi_1$  yields the composite solution

$$\begin{aligned} \phi_1 = & 3 \tanh^2 \left( \sqrt{\frac{\bar{\text{Er}}}{2}} z + \tanh^{-1} \sqrt{\frac{2 + \Phi_0}{3}} \right) - 3 \tanh^2 \left( \sqrt{\frac{\bar{\text{Er}}}{2}} (1 - z) + \tanh^{-1} \sqrt{\frac{2 - \Phi_0}{3}} \right) \\ & + \phi_{\text{inner}} \left( \bar{\text{Er}}^{1/3} \left( z - \frac{1}{2} \right) \right) + O(\bar{\text{Er}}^{-1}), \end{aligned} \quad (61)$$

where  $\Phi_0$  satisfies (59) subject to the initial condition  $\Phi_0(0) = \theta$ .

## E. The Director Angle at the Boundaries

As we have already seen, the leading-order director angle at the boundaries  $\Phi_0$  satisfies the singular ordinary differential equation (59) subject to the initial condition  $\Phi_0(0) = \theta$ . Inspection of (59) reveals that  $\Phi_0$  rapidly evolves towards its constant steady state value of  $\Phi_{\text{0SS}}$  given by

$$\Phi_0 = \Phi_{\text{0SS}} = \frac{2}{3} \left[ k - |\chi|^{1/3} \cos \left( \frac{1}{3} \arg(\chi) \right) \right]^2 - 2 + O(\bar{\text{Er}}^{-1}) \quad (62)$$

over a short timescale of  $O(\bar{\text{Er}}^{-1/2}) \ll 1$ . Rescaling  $t$  appropriately according to  $t = \bar{\text{Er}}^{-1/2} \hat{t}$  shows that this rapid evolution is described by the implicit solution

$$-\sqrt{\frac{2}{3}} \hat{t} = a \log \left( \frac{\sqrt{2 + \Phi_0} - v_1}{\sqrt{2 + \theta} - v_1} \right) + b \log \left( \frac{\sqrt{2 + \Phi_0} - v_2}{\sqrt{2 + \theta} - v_2} \right) + c \log \left( \frac{\sqrt{2 + \Phi_0} - v_3}{\sqrt{2 + \theta} - v_3} \right), \quad (63)$$

where

$$a = \frac{2v_1}{(v_1 - v_2)(v_1 - v_3)}, \quad b = \frac{2v_2}{(v_2 - v_1)(v_2 - v_3)}, \quad c = \frac{2v_3}{(v_3 - v_1)(v_3 - v_2)}. \quad (64)$$

The constants  $v_1$ ,  $v_2$ , and  $v_3$  are the roots of the cubic polynomial

$$\mathcal{F}(v) = v^3 + \sqrt{6}kv^2 - 3v - 2\sqrt{6}k, \quad (65)$$

which can be written explicitly as

$$v_1 = -\sqrt{\frac{2}{3}} \left[ k - |\chi|^{1/3} \cos \left( \frac{1}{3} \arg(\chi) \right) \right], \quad (66)$$

$$v_2 = -\sqrt{\frac{2}{3}} \left[ k + |\chi|^{1/3} \cos \left( \frac{1}{3} \arg(\chi) - \frac{\pi}{3} \right) \right], \quad (67)$$

$$v_3 = -\sqrt{\frac{2}{3}} \left[ k + |\chi|^{1/3} \cos \left( \frac{1}{3} \arg(\chi) + \frac{\pi}{3} \right) \right], \quad (68)$$

where  $|\chi|$  and  $\arg(\chi)$  are the modulus and argument, respectively, of the complex number  $\chi$ , defined by

$$\chi = 18k - 8k^3 + 6i\sqrt{6 + 3k^2 + 16k^4}. \quad (69)$$

It is informative to consider three cases for the size of the parameter  $k$  (and hence for the relative size of the non-dimensional groups  $\bar{\text{Er}}$  and  $\mathcal{A}$ ) in which further analytical progress can be made. Specifically, we consider the cases  $k \gg 1$  ( $\mathcal{A} \gg \bar{\text{Er}}^{1/2} \gg 1$ ),  $k \ll 1$  (either  $\bar{\text{Er}}^{1/2} \gg \mathcal{A} \gg 1$  or  $\bar{\text{Er}}^{1/2} \gg 1 \gg \mathcal{A}$ ), and  $k = O(1)$  ( $\bar{\text{Er}}^{1/2} = O(\mathcal{A}) \gg 1$ ).



1. *The case  $k \gg 1$*

In the case  $k \gg 1$  ( $\mathcal{A} \gg \bar{\text{Er}}^{1/2} \gg 1$ ) the implicit solution (63) reduces to the simple explicit solution

$$\Phi_0 = \theta e^{-2k\hat{t}}, \quad \text{i.e.} \quad \Phi_0 = \theta e^{-2\mathcal{A}t}, \quad (70)$$

which approaches its steady state value  $\Phi_{\text{OSS}} = 0$  as  $t \rightarrow \infty$ , i.e. the director at the boundaries becomes planar as  $t \rightarrow \infty$ . This case represents a regime in which the anchoring is sufficiently strong that the effects of flow are negligible at the boundaries, and the (non-dimensional) timescale of the evolution of the director at the boundaries towards its steady state value, denoted by  $\sigma$ , is given by

$$\sigma = \frac{1}{2\mathcal{A}} \ll 1. \quad (71)$$

2. *The case  $k \ll 1$*

In the case  $k \ll 1$  (either  $\bar{\text{Er}}^{1/2} \gg \mathcal{A} \gg 1$  or  $\bar{\text{Er}}^{1/2} \gg 1 \gg \mathcal{A}$ ) the implicit solution (63) reduces to the appropriate explicit solution

$$\Phi_0 = -2 + 3 \tanh \left( \sqrt{\frac{1}{2}} \hat{t} + \tanh^{-1} \sqrt{\frac{2+\theta}{3}} \right)^2, \quad (72)$$

which approaches its steady state value  $\Phi_{\text{OSS}} = 1$  as  $t \rightarrow \infty$ , i.e. the director angle at the boundaries approaches the Leslie angle as  $t \rightarrow \infty$ , according to

$$\Phi_0 = 1 - 12 \exp \left[ -2 \tanh \sqrt{\frac{2+\theta}{3}} - \sqrt{2} \bar{\text{Er}}^{1/2} t \right] + O \left( \exp \left[ -2 \bar{\text{Er}}^{1/2} t \right] \right). \quad (73)$$

This case represents a regime in which the flow is sufficiently strong that the effects of anchoring are negligible at the boundaries, and the timescale  $\sigma$  is given by

$$\sigma = \frac{1}{\sqrt{2} \bar{\text{Er}}^{1/2}} \ll 1. \quad (74)$$

3. *The case  $k = O(1)$*

In the case  $k = O(1)$  ( $\bar{\text{Er}}^{1/2} = O(\mathcal{A}) \gg 1$ ) the implicit solution (63) approaches its steady state value  $\Phi_{\text{OSS}}$  ( $0 < \Phi_{\text{OSS}} < 1$ ) given by (62) as  $t \rightarrow \infty$ . Unfortunately (63) does not yield an explicit expression for the timescale  $\sigma$ . However, as we shall show in Section VIB,  $\sigma$  is always less than both (71) and (74), and so (71) and (74) provide an upper bound on  $\sigma$  for all values of  $k$ . This case represents a regime in which the effects of anchoring and flow are comparable at the boundaries, and hence the behaviour of the director at the boundaries depends on a combination of these two effects.

## V. ASYMPTOTIC SOLUTION IN THE LIMIT OF SMALL ERICKSEN NUMBER

In the limit of small Ericksen number  $\bar{E}r \rightarrow 0$  we seek an asymptotic solution for  $\phi_1$  in powers of  $\bar{E}r$  when  $\epsilon \ll \bar{E}r \ll 1$  in the form  $\phi_1 = \phi_{1,0} + \bar{E}r \phi_{1,1} + O(\bar{E}r^2)$ , where  $\phi_{1,0}$  denotes the term that is first order in  $\epsilon$  and leading order in  $\bar{E}r$  and  $\phi_{1,1}$  denotes the term that is first order in  $\epsilon$  and first order in  $\bar{E}r$ .

At leading order in  $\bar{E}r$  the director angle equation (49) reduces to simply

$$\frac{\partial^2 \phi_{1,0}}{\partial z^2} = 0, \quad (75)$$

subject to the dissipative weak anchoring conditions (50) and (51)

$$\frac{\partial \phi_{1,0}}{\partial t} = + \frac{\partial \phi_{1,0}}{\partial z} - 2\mathcal{A}\phi_{1,0} \quad \text{at } z = 0, \quad (76)$$

$$\frac{\partial \phi_{1,0}}{\partial t} = - \frac{\partial \phi_{1,0}}{\partial z} - 2\mathcal{A}\phi_{1,0} \quad \text{at } z = 1, \quad (77)$$

and the initial conditions (52) and (53)  $\phi_{1,0}(0,0) = +\theta$  and  $\phi_{1,0}(1,0) = -\theta$ . Integrating (75) twice with respect to  $z$ , using (76) and (77) and the initial conditions on  $\phi_{1,0}$ , yields the solution for  $\phi_{1,0}$ , namely

$$\phi_{1,0} = \theta(1 - 2z) e^{-2(1+\mathcal{A})t}. \quad (78)$$

At first order in  $\bar{E}r$  the director angle equation (49) reduces to

$$\frac{\partial^2 \phi_{1,1}}{\partial z^2} = (2z - 1)(1 - \phi_{1,0}^2), \quad (79)$$

subject to the dissipative weak anchoring conditions (50) and (51)

$$\frac{\partial \phi_{1,1}}{\partial t} = + \frac{\partial \phi_{1,1}}{\partial z} - 2\mathcal{A}\phi_{1,1} \quad \text{at } z = 0, \quad (80)$$

$$\frac{\partial \phi_{1,1}}{\partial t} = - \frac{\partial \phi_{1,1}}{\partial z} - 2\mathcal{A}\phi_{1,1} \quad \text{at } z = 1, \quad (81)$$

and the initial conditions (52) and (53)  $\phi_{1,1}(0,0) = 0$  and  $\phi_{1,1}(1,0) = 0$ . Integrating (79) twice with respect to  $z$ , using (78), (80) and (81) and the initial conditions on  $\phi_{1,1}$ , yields the solution for  $\phi_{1,1}$ , namely

$$\begin{aligned} \phi_{1,1} = \frac{2z-1}{60} & \left[ 5 \left( 2z^2 - 2z - \frac{1}{1+\mathcal{A}} \right) + \frac{5+3\theta^2}{1+\mathcal{A}} e^{-2(1+\mathcal{A})t} \right. \\ & \left. + 3\theta^2 \left( 4z^4 - 8z^3 + 6z^2 - 2z + \frac{1}{1+\mathcal{A}} \right) e^{-4(1+\mathcal{A})t} \right]. \end{aligned} \quad (82)$$

Using (78) and (82) the asymptotic solution for  $\phi_1$  is therefore

$$\begin{aligned} \phi_1 = \theta(1 - 2z)e^{-2(1+\mathcal{A})t} & + \frac{2z-1}{60} \left[ 5 \left( 2z^2 - 2z - \frac{1}{1+\mathcal{A}} \right) + \frac{5+3\theta^2}{1+\mathcal{A}} e^{-2(1+\mathcal{A})t} \right. \\ & \left. + 3\theta^2 \left( 4z^4 - 8z^3 + 6z^2 - 2z + \frac{1}{1+\mathcal{A}} \right) e^{-4(1+\mathcal{A})t} \right] \bar{E}r + O(\bar{E}r^2), \end{aligned} \quad (83)$$

and hence the asymptotic solution for the director angle at the boundaries  $\Phi$  is

$$\Phi = \theta e^{-2(1+\mathcal{A})t} + \frac{1}{60(1+\mathcal{A})} \left[ 5 - (5+3\theta^2) e^{-2(1+\mathcal{A})t} - 3\theta^2 e^{-4(1+\mathcal{A})t} \right] \bar{E}r + O(\bar{E}r^2). \quad (84)$$

In particular, from (83) the steady state solution  $\phi_{1SS}$  is given by

$$\phi_{1SS} = \frac{2z-1}{12} \left[ 2z^2 - 2z - \frac{1}{1+\mathcal{A}} \right] \bar{E}r + O(\bar{E}r^2), \quad (85)$$

and from either (84) or (85) the steady state value  $\Phi_{SS}$  is given by

$$\Phi_{SS} = \frac{\bar{E}r}{12(1+\mathcal{A})} + O(\bar{E}r^2). \quad (86)$$

In particular, the solution for the director angle given by (83) and (84) is dominated by splay elastic effects with viscous effects appearing at  $O(\bar{E}r) \ll 1$ . In addition, from (84) the timescale  $\sigma$  is given by

$$\sigma = \frac{1}{2(1+\mathcal{A})}. \quad (87)$$

Note that even in the special case  $\mathcal{A} = 0$  in which case there is no anchoring force in (50) and (51), there is still an elastic restoring force due to the  $\partial\phi_1/\partial z$  term, and hence the director angle at the boundaries still rotates such that  $\Phi \rightarrow \Phi_{SS} = \bar{E}r/12 + O(\bar{E}r^2)$  as  $t \rightarrow \infty$ .

## VI. SOLUTIONS FOR GENERAL VALUES OF THE ERICKSEN NUMBER

In this section we obtain numerical solutions of the director angle equation (49) subject to (50)–(53) for general values of the Ericksen number and, in particular, compare them with the quasi-steady asymptotic solutions in the limits of large and small  $\bar{E}r$  described in Sections IV and V, respectively. The numerical approach we adopt uses the MATLAB boundary value problem solver *bvp4c* [52] with an implicit Euler method for approximating the time derivatives in (50) and (51). In all of our numerical calculations the simulation time is chosen to be six times longer than the appropriate timescale given by (71), (74) or (87) in order to allow sufficient time for convergence to the steady state solution. In all of the numerical calculations reported here use the value  $\theta = 0.5$  for the initial value of the director angle at the boundaries.

### A. The Director Angle

Figure 4(a) shows the initial director angle  $\phi_1(z, 0)$  and Figure 4(b) shows the steady state solution for the director angle  $\phi_{1SS}(z)$ , both plotted as functions of  $z$  according to the numerical solution (solid lines) when  $\bar{E}r = 10^{-1}$ ,  $\bar{E}r = 10$ ,  $\bar{E}r = 10^2$  and  $\bar{E}r = 10^4$ , the large  $\bar{E}r$  asymptotic solution (dashed lines) given by (61) when  $\bar{E}r = 10^2$  and  $\bar{E}r = 10^4$ , and the small  $\bar{E}r$  asymptotic solution (dotted lines) given by (83) when  $\bar{E}r = 10^{-1}$  and  $\bar{E}r = 10$ . The insets in Figure 4 show the corresponding results for an intermediate value of  $\bar{E}r$ , namely  $\bar{E}r = 50$ . In particular, Figure 4 shows how the leading-order velocity in the channel  $u_0$  given by (48) affects both the initial director angle and the steady state director angle. Specifically, as described in Section II C, in the lower half of the channel the positive shear rate ( $\partial u_0/\partial z > 0$ ) rotates the director angle towards the positive Leslie angle  $\phi_1 = +1$ , while in the upper half of the channel the negative shear rate ( $\partial u_0/\partial z < 0$ ) rotates it towards the negative Leslie angle  $\phi_1 = -1$ . When  $\bar{E}r$  is large (e.g. when  $\bar{E}r = 10^4$ ), the behaviour of the director is dominated by viscous effects, with flow alignment at either the positive or the negative Leslie angle except for within the narrow reorientational boundary and internal layers

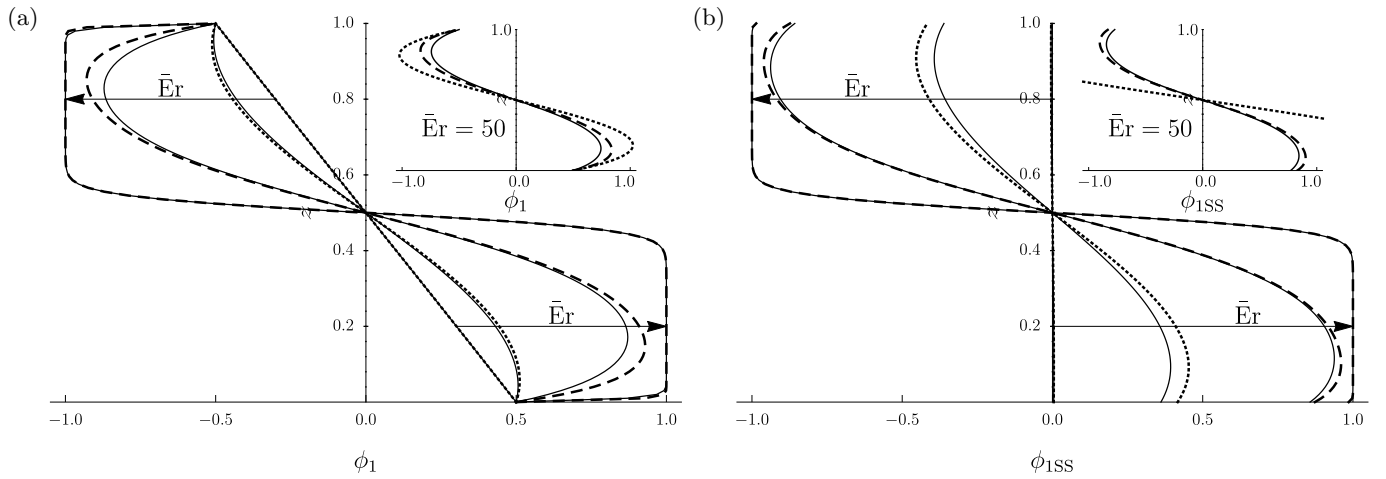


FIG. 4. (a) The initial director angle  $\phi_1(z, 0)$  and (b) the steady state solution for the director angle  $\phi_{1SS}(z)$  plotted as functions of  $z$  for  $\mathcal{A} = 1$  and  $\theta = 0.5$  according to the numerical solution (solid lines) when  $\bar{E}r = 10^{-1}$ ,  $\bar{E}r = 10$ ,  $\bar{E}r = 10^2$  and  $\bar{E}r = 10^4$ , the large  $\bar{E}r$  asymptotic solution (dashed lines) given by (61) when  $\bar{E}r = 10^2$  and  $\bar{E}r = 10^4$ , and the small  $\bar{E}r$  asymptotic solution (dotted lines) given by (83) when  $\bar{E}r = 10^{-1}$  and  $\bar{E}r = 10$ . In both (a) and (b) the insets show the corresponding results when  $\bar{E}r = 50$ . The arrows show the direction of increasing  $\bar{E}r$ .

at leading order in the limit of large  $\bar{E}r$ , as described in Section IV. When  $\bar{E}r$  is small (e.g. when  $\bar{E}r = 10^{-1}$ ), the behaviour of the director is dominated by splay elastic effects, with viscous effects appearing at first order in the limit of small  $\bar{E}r$ , as described in Section V. Figure 4 also shows that as  $\bar{E}r$  varies there is a continuous transition between the asymptotic behaviour for large  $\bar{E}r$  and that for small  $\bar{E}r$  and that, in fact, the two asymptotic solutions capture the behaviour of  $\phi_1$  rather well for all values of  $\bar{E}r$ . This continuous transition is rather different to the discontinuous transitions observed in channel flow of a nematic with homeotropic anchoring by Sengupta et al. [39], Anderson et al. [40], Crespo et al. [41], and Batista et al. [42].

Figure 5 shows the director angle  $\phi_1(z, t)$  plotted as a function of  $z$  for various times  $t$  according to (a) the numerical solution (solid lines) and the large  $\bar{E}r$  asymptotic solution (dashed lines) when  $\bar{E}r = 10^4$ , (b) the numerical solution (solid lines) when  $\bar{E}r = 50$ , and (c) the numerical solution (solid lines) and the small  $\bar{E}r$  asymptotic solution (dotted lines) when  $\bar{E}r = 10^{-1}$ . In each part of Figure 5 the final time plotted is chosen so that the solution is close to its steady state solution  $\phi_{1SS}$  shown in Figure 4(b). In particular, Figure 5 illustrates that  $\phi_1$  always approaches its steady state solution  $\phi_{1SS}$  monotonically as  $t \rightarrow \infty$ .

Figure 6 shows the director angle at the boundaries  $\Phi$  plotted as a function of time  $t$  according to the numerical solution (solid lines) when  $\bar{E}r = 10^{-1}$ ,  $\bar{E}r = 10$ ,  $\bar{E}r = 50$ ,  $\bar{E}r = 10^2$  and  $\bar{E}r = 10^4$ , the large  $\bar{E}r$  asymptotic solution (dashed lines) when  $\bar{E}r = 10^2$  and  $\bar{E}r = 10^4$ , and the small  $\bar{E}r$  asymptotic solution (dotted lines) when  $\bar{E}r = 10^{-1}$ ,  $\bar{E}r = 10$ . In particular, Figure 6 illustrates that  $\Phi$  always approaches its steady state value  $\Phi_{SS}$  monotonically from above when  $\Phi_{SS} < \theta$  and from below when  $\Phi_{SS} > \theta$  as  $t \rightarrow \infty$ , and that  $\Phi_{SS}$  is a monotonically increasing function of  $\bar{E}r$ .

Figures 5 and 6 also illustrate that the approach to the steady state solution gets monotonically faster as  $\bar{E}r$  is increased. This behaviour will be analysed in more detail in Section VI B.

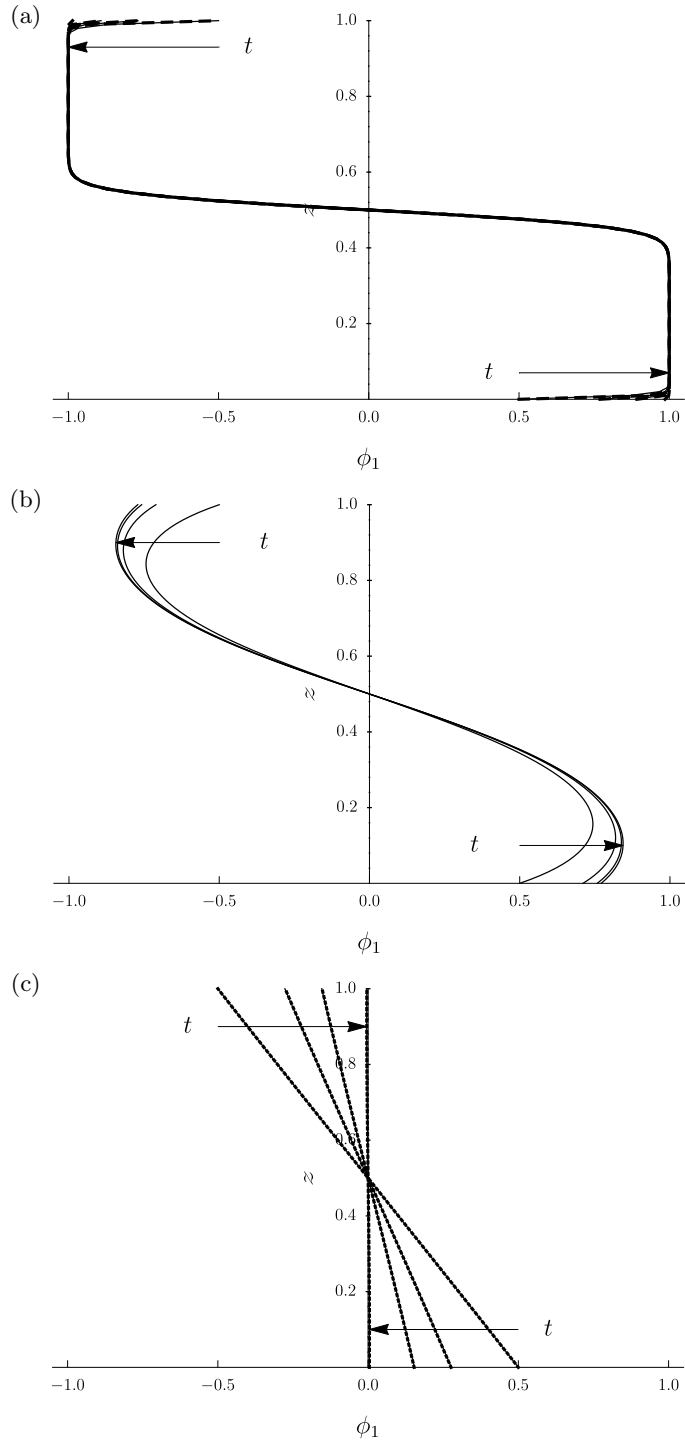


FIG. 5. The director angle  $\phi_1(z, t)$  plotted as a function of  $z$  for  $\mathcal{A} = 1$  and  $\theta = 0.5$  according to (a) the numerical solution (solid lines) and the (barely visible) large  $\bar{Er}$  asymptotic solution (dashed lines) given by (61) when  $\bar{Er} = 10^4$  for  $t = 0.0$ ,  $t = 0.006$ ,  $t = 0.012$ , and  $t = 0.06$ , (b) the numerical solution (solid lines) when  $Er = 50$  for  $t = 0.0$ ,  $t = 0.15$ ,  $t = 0.3$  and  $t = 3.0$ , and (c) the numerical solution (solid lines) and the (barely visible) small  $\bar{Er}$  asymptotic solution (dotted lines) given by (83) when  $\bar{Er} = 10^{-1}$  for  $t = 0.0$ ,  $t = 0.15$ ,  $t = 0.3$  and  $t = 3.0$ . The arrows show the direction of increasing  $t$ .

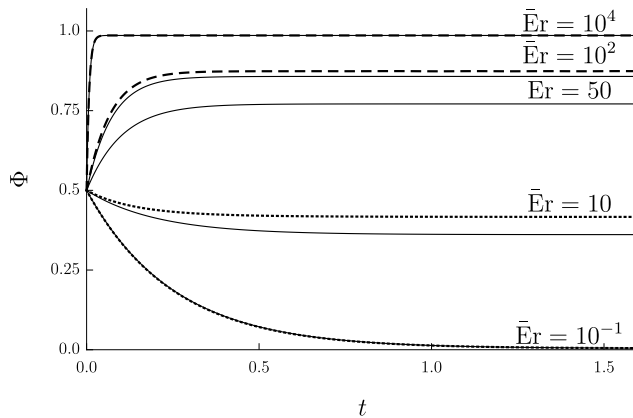


FIG. 6. The director angle at the boundaries  $\Phi$  plotted as a function of time  $t$  for  $\mathcal{A} = 1$  and  $\theta = 0.5$  according to the numerical solution (solid lines) when  $\bar{E}r = 10^{-1}$ ,  $\bar{E}r = 10$ ,  $\bar{E}r = 50$ ,  $\bar{E}r = 10^2$  and  $\bar{E}r = 10^4$ , the large  $\bar{E}r$  asymptotic solution (dashed lines) given by (63) when  $\bar{E}r = 10^2$  and  $\bar{E}r = 10^4$ , and the small  $\bar{E}r$  asymptotic solution (dotted lines) given by (84) when  $\bar{E}r = 10^{-1}$ ,  $\bar{E}r = 10$ .

Figure 7 shows the steady state value the director angle at the boundaries  $\Phi_{SS}$  plotted as a function of the Ericksen number  $\bar{E}r$  according to the numerical solution (solid lines), the large  $\bar{E}r$  asymptotic solution given by (62) (dashed lines), and the small  $\bar{E}r$  asymptotic solution (dotted lines) given by (86) for various values of  $\mathcal{A}$ . In particular, Figure 7 illustrates that  $\Phi_{SS}$  is a monotonically decreasing function of  $\mathcal{A}$ . Figure 7 also confirms that the numerical solutions for  $\Phi_{SS}$  for large and small values of  $\bar{E}r$  are in excellent agreement with the asymptotic solutions in the limits  $\bar{E}r \rightarrow \infty$  and  $\bar{E}r \rightarrow 0$  given in Sections IV and V, respectively. Moreover, as we have already seen, in the former limit the leading-order expression for the value of  $\Phi_{SS}$  depends on  $\bar{E}r$  and  $\mathcal{A}$  only in the combination  $k = \mathcal{A}/\bar{E}r^{1/2}$ , and hence the curves for  $\Phi_{SS}$  for large values of  $\bar{E}r$  are simply appropriately horizontally stretched versions of each other, and as Figure 7 illustrates, the range of validity of this expression widens as  $\mathcal{A}$  increases.

## B. The Timescale $\sigma$

In order to extract the timescale  $\sigma$  introduced in Section VIA from the numerical solutions we fitted the numerical solutions for  $\Phi_{SS}$  with a function of  $t$  of the form

$$\log |\Phi_{SS} - \Phi| = C - \frac{t}{\sigma}, \quad (88)$$

where  $C = C(\theta)$  is a function of the initial director angle at the boundaries only. In particular, this procedure recovers the asymptotic expressions for  $\sigma$  derived in Sections IV E and V, namely (71), (74) and (87).

Figure 8 shows  $\sigma$  plotted as a function of  $\bar{E}r$  extracted from the numerical solution using (88) and according to the large  $\bar{E}r$  asymptotic solution when  $k \ll 1$  given by (74) and the small  $\bar{E}r$  asymptotic solution given by (87). (Note that, for clarity, the timescale according to the large  $\bar{E}r$  asymptotic solution when  $k \gg 1$ , namely  $\sigma = 1/(2\mathcal{A})$ , is omitted from Figure 8 as it is virtually indistinguishable from  $\sigma = 1/(2(1 + \mathcal{A}))$ .) In particular, Figure 8 shows that  $\sigma$  is a monotonically decreasing function of  $\bar{E}r$ , and that as  $\bar{E}r$  varies there is a continuous transition between

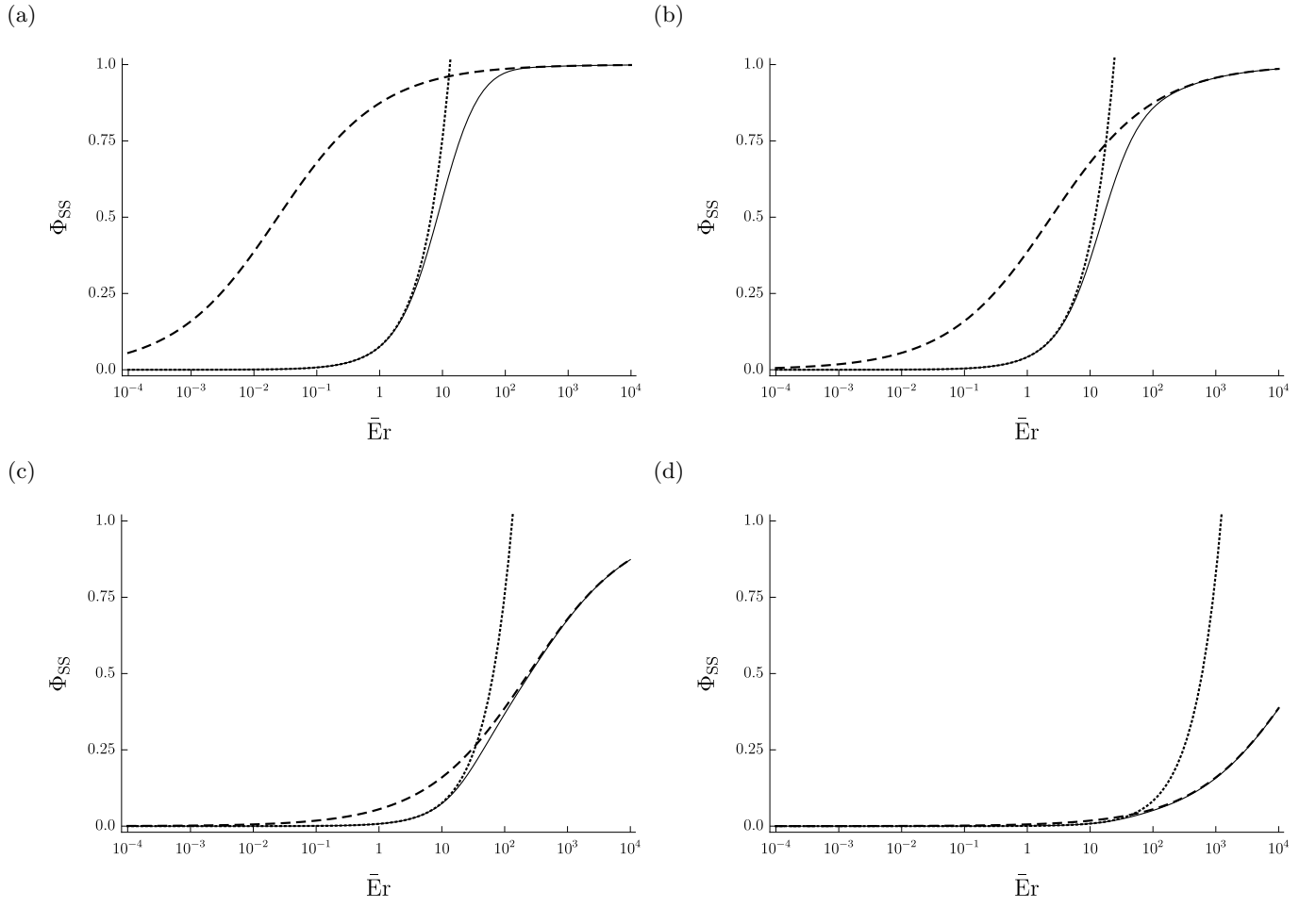


FIG. 7. The steady state value of the director angle at the boundaries  $\Phi_{SS}$  plotted as a function of the Ericksen number  $\bar{E}r$  according to the numerical solution (solid lines), the large  $\bar{E}r$  asymptotic solution (dashed lines) given by (62), and the small  $\bar{E}r$  asymptotic solution (dotted lines) given by (86) for (a)  $\mathcal{A} = 10^{-1}$ , (b)  $\mathcal{A} = 1$ , (c)  $\mathcal{A} = 10$ , and (d)  $\mathcal{A} = 10^2$ .

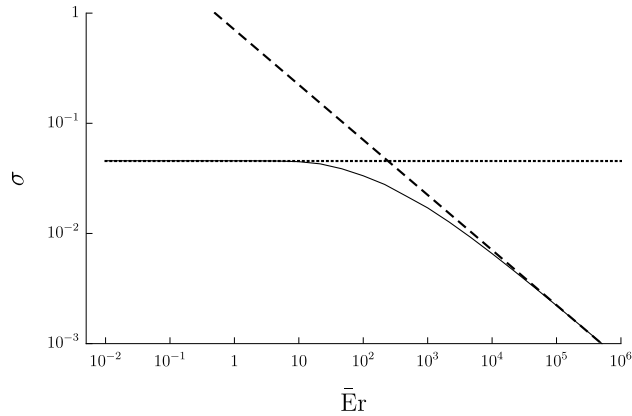


FIG. 8. The timescale  $\sigma$  plotted as a function of the Ericksen number  $\bar{E}r$  extracted from the numerical solution using (88) (solid line) and according to the large  $\bar{E}r$  asymptotic solution when  $k \ll 1$  (dashed line) given by (74) and the small  $\bar{E}r$  asymptotic solution (dotted line) given by (87) for  $\mathcal{A} = 10$  and  $\theta = 0.5$ .

	$\bar{E}r \rightarrow \infty$			$\bar{E}r \rightarrow 0$
	$k \gg 1$	$k = O(1)$	$k \ll 1$	
$\Phi_{SS}$	0	Equation (62)	1	$\frac{\bar{E}r}{12(\mathcal{A} + 1)} \ll 1$
$\sigma$	$\frac{1}{2\mathcal{A}} \ll 1$	( $\star$ )	$\frac{1}{\sqrt{2}\bar{E}r^{1/2}} \ll 1$	$\frac{1}{2(\mathcal{A} + 1)}$

TABLE II. The steady state value for the director angle at the boundaries  $\Phi_{SS}$  and the timescale  $\sigma$  in the asymptotic limit of large  $\bar{E}r$  in the cases  $k \gg 1$ ,  $k = O(1)$  and  $k \ll 1$ , where  $k = \mathcal{A}/\bar{E}r^{1/2}$ , and in the asymptotic limit of small  $\bar{E}r$ . The star ( $\star$ ) denotes that, while there is no explicit expression for  $\sigma$  in this case, the expressions for  $k \gg 1$  and  $k \ll 1$  provide a upper bound on  $\sigma$  for all values of  $k$ .

$\sigma = 1/(\sqrt{2}\bar{E}r^{1/2}) = O(\bar{E}r^{-1/2}) \ll 1$  for large values of  $\bar{E}r$  and  $\sigma = 1/(2(1 + \mathcal{A})) = O(1)$  for small values of  $\bar{E}r$ . Moreover, Figure 8 also shows, as mentioned in Section IV E 3, that  $\sigma$  is always less than both (71) and (74), and so (71) and (74) provide a upper bound on  $\sigma$  for all values of  $\bar{E}r$ .

## VII. CONCLUSIONS

Motivated by the ODF method for the industrial manufacturing of LCDs, in the present work we analysed pressure-driven flow of a nematic in a channel with dissipative weak planar anchoring at the boundaries of the channel. We obtained quasi-steady asymptotic solutions for the director angle  $\phi$  and the velocity  $u$  in the limit of small Leslie angle, in which case the key parameters are the Ericksen number  $\bar{E}r$  and the anchoring strength parameter  $\mathcal{A}$ . In the limit of large Ericksen number  $\bar{E}r \rightarrow \infty$  the solution for the director angle has narrow reorientational boundary layers of width  $O(\bar{E}r^{-1/2}) \ll 1$  near  $z = 0$  and  $z = 1$  and a narrow reorientational internal layer of width  $O(\bar{E}r^{-1/3}) \ll 1$  near  $z = 1/2$  separated by two outer regions in which the director is aligned at the positive Leslie angle in the lower half of the channel and the negative Leslie angle in the upper half of the channel. On the other hand, in the limit of small Ericksen number  $\bar{E}r \rightarrow 0$  the solution for the director angle given by (83) and (84) is dominated by splay elastic effects with viscous effects appearing at  $O(\bar{E}r) \ll 1$ . As  $\bar{E}r$  varies there is a continuous transition between these asymptotic behaviours and, in fact, the two asymptotic solutions capture the behaviour rather well for all values of  $\bar{E}r$ . The steady state value of the director angle at the boundaries  $\Phi_{SS}$  and the timescale of the evolution towards this steady state value  $\sigma$  in the asymptotic limits of large and small  $\bar{E}r$  are summarised in Table II. In particular, the values of  $\sigma$  in Table II correspond to the dimensional boundary director rotation timescale  $\sigma\tau_4$  given by

$$\sigma\tau_4 \sim \gamma_S \times \begin{cases} \frac{1}{2\mathcal{A}} & \text{for } \bar{E}r \gg 1 \text{ and } k \gg 1, \\ \sqrt{\frac{-(\alpha_4 + \alpha_6)}{2(\alpha_2\alpha_3)^{1/2}GhK_1}} & \text{for } \bar{E}r \gg 1 \text{ and } k \ll 1, \\ \frac{h}{2(K_1 + Ah)} & \text{for } \bar{E}r \ll 1. \end{cases} \quad (89)$$



Using the estimated parameter values for the ODF method given Section IID gives  $\bar{E}r = 1.7 \times 10^2$ ,  $\mathcal{A} = 1-10^2$  and hence  $k = 0.08-8$ , suggesting that the regimes in which  $\bar{E}r \gg 1$  and  $k \ll 1$  or  $k = O(1)$  are probably the most relevant to the ODF method. Hence (89) yields a dimensional boundary director rotation timescale of  $\sigma\tau_4 \simeq 5 \times 10^{-3}$  s or less, which is substantially shorter than the dimensional timescale of the ODF method of  $\tau_{\text{ODF}} = 10^{-1}$  s, suggesting that there is sufficient time for significant transient flow-driven distortion of the nematic molecules at the substrates from their required orientation to occur, which could lead to the formation of ODF mura. An obvious conclusion is that this distortion could, in theory, be reduced by decreasing  $\bar{E}r$  and/or increasing  $\mathcal{A}$  by, for example, reducing the speed at which the substrates are squeezed together and/or increasing the strength of the adhesion between the alignment layer and the nematic, however the extent to which either of these are realistic options in practice is not clear. It should, however, be noted that once the squeezing stops, and hence the flow of the nematic virtually ceases (so that  $\bar{E}r$  becomes very small), then (89) yields a dimensional boundary director rotation timescale of approximately  $\sigma\tau_4 \simeq 2.5 \times 10^{-2}$  s or less, which means that the flow-driven distortion of the nematic molecules relaxes almost immediately. The remaining issue is, therefore, whether the significant transient flow-driven distortion of the nematic molecules described in the present work causes permanent or semi-permanent flow-driven misalignment of the orientation of the molecules in the alignment layers. Answering this question could lead to further understanding of ODF mura but requires more detailed modelling of the molecules in the alignment layers, and so is beyond the scope of the present work.

Finally, mentioned in Section IIA, the present analysis of dissipative weak planar anchoring is not directly relevant to devices with homeotropic anchoring, such as VAN devices, or to devices in which the director does not remain in the  $(x, z)$  plane, such as TN or STN devices. However, in such devices flow alignment towards the (typically small) Leslie angle involves a much larger rotation of the director than that described in the present work, and so we suspect that such devices are even more susceptible to flow-driven misalignment of the director at the boundaries during filling than those studied in the present work.

## ACKNOWLEDGMENTS

This work was supported by the United Kingdom Engineering and Physical Sciences Research Council (EPSRC), the University of Strathclyde, and Merck KGaA via EPSRC research grant number EP/P51066X/1. The authors gratefully acknowledge the assistance of Dr David J. Allwright of the Smith Institute for helping to facilitate the present collaboration between the University of Strathclyde and Merck KGaA.

- 
- [1] Y. Yamamoto. LCD processing and testing. In J. Chen, W. Cranton, and M. Fihn, editors, *Handbook of Visual Display Technology*, chapter 7.6.1, pages 1649–1671. Springer, 2012.
  - [2] H. Kamiya, K. Tajima, K. Toriumi, K. Terada, H. Inoue, T. Yokoue, N. Shimizu, T. Kobayashi, S. Odahara, G. Hougham, C. Cai, J. H. Glownia, R. J. von Gutfeld, R. John, and S.-C. A. Lien. 56.3: Development of One Drop Fill technology for AM-LCDs. *Society for Information Display International Symposium Digest of Technical Papers*, 32(1):1354–1357, 2001.
  - [3] A. Hirai, I. Abe, M. Mitsumoto, and S. Ishida. One Drop Filling for liquid crystal display panel produced for larger-sized

- mother glass. *Hitachi Review*, 57(3):144–148, 2008.
- [4] K.-C. Fan, J.-Y. Chen, C.-H. Wang, and W.-C. Pan. Development of a drop-on-demand droplet generator for one-drop-fill technology. *Sensors and Actuators A: Physical*, 147(2):649–655, 2008.
- [5] W. K. Pratt, S. S. Sawkar, and K. O’Reilly. Automatic blemish detection in liquid crystal flat panel displays. *Proceedings of SPIE*, 3306:1–12, 1998.
- [6] H. Lee, S. Song, J. Lee, A. Xiao, T. Min, and S. Su. 9.3: Analysis of liquid crystal drop mura in high resolution mobile thin film transistor liquid crystal displays. *Society for Information Display International Symposium Digest of Technical Papers*, 45(1):97–99, 2014.
- [7] J. R. L. Cousins, S. K. Wilson, N. J. Mottram, D. Wilkes, L. Weegels, and K. Lin. LCT8-4: A model for the formation of mura during the One-Drop-Filling process. In *Proceedings of the 25th International Display Workshops (IDW 2018)*, volume 1, pages 125–127. Society for Information Display, 2018.
- [8] J. R. L. Cousins, S. K. Wilson, N. J. Mottram, D. Wilkes, and L. Weegels. Squeezing a drop of nematic liquid crystal with strong elasticity effects. *Physics of Fluids*, 31(8):083107, 2019.
- [9] D. Armitage, I. Underwood, and S.-T. Wu. Transmissive liquid crystal microdisplays. In *Introduction to Microdisplays*, chapter 5, pages 149–172. John Wiley & Sons, Ltd, 2006.
- [10] L. P. Jones. Alignment properties of liquid crystals. In J. Chen, W. Cranton, and M. Fihn, editors, *Handbook of Visual Display Technology*, chapter 7.2.2, pages 1387–1402. Springer, 2012.
- [11] K. Hanaoka, Y. Nakanishi, Y. Inoue, S. Tanuma, Y. Koike, and K. Okamoto. 40.1: A new MVA-LCD by polymer sustained alignment technology. *Society for Information Display International Symposium Digest of Technical Papers*, 35(1):1200–1203, 2004.
- [12] H. Yoshida. Vertically Aligned Nematic (VAN) LCD technology. In J. Chen, W. Cranton, and M. Fihn, editors, *Handbook of Visual Display Technology*, chapter 7.3.4, pages 1485–1505. Springer, 2012.
- [13] L. Weng, P.-C. Liao, C.-C. Lin, T.-L. Ting, W.-H. Hsu, J.-J. Su, and L.-C. Chien. Anchoring energy enhancement and pretilt angle control of liquid crystal alignment on polymerized surfaces. *AIP Advances*, 5(9):097218, 2015.
- [14] W. M. Gibbons, P. J. Shannon, S.-T. Sun, and B. J. Swetlin. Surface-mediated alignment of nematic liquid crystals with polarized laser light. *Nature*, 351:49–50, 1991.
- [15] J. L. Ericksen. Anisotropic fluids. *Archive for Rational Mechanics and Analysis*, 4:231–237, 1959.
- [16] F. M. Leslie. Some constitutive equations for anisotropic fluids. *Quarterly Journal of Mechanics and Applied Mathematics*, 19(3):357–370, 1966.
- [17] I. W. Stewart. *The Static and Dynamic Continuum Theory of Liquid Crystals*. Taylor & Francis, 2004.
- [18] N. J. Mottram and C. J. P. Newton. Introduction to Q-tensor theory. *arXiv preprint arXiv:1409.3542*, 2014.
- [19] A. N. Beris and B. J. Edwards. *Thermodynamics of Flowing Systems: with Internal Microstructure*. Oxford University Press, 1994.
- [20] C. Zannoni. Computer simulation and molecular design of model liquid crystals. In Fabbrizzi L. and Poggi A., editors, *Chemistry at the Beginning of the Third Millennium*, pages 329–342. Springer, 2000.
- [21] N. J. Mottram and C. J. P. Newton. Liquid crystal theory and modelling. In J. Chen, W. Cranton, and M. Fihn, editors, *Handbook of Visual Display Technology*, chapter 7.2.3, pages 1403–1429. Springer, 2012.
- [22] A. Rapini and M. Papoular. Distorsion d’une lamelle nématique sous champ magnétique conditions d’ancrage aux parois. *Journal de Physique Colloque*, 30(C4):C4–54–C4–56, 1969.
- [23] H. Yokoyama and H. A. van Sprang. A novel method for determining the anchoring energy function at a nematic liquid crystal-wall interface from director distortions at high fields. *Journal of Applied Physics*, 57(10):4520–4526, 1985.
- [24] Yu. A. Nastishin, R. D. Polak, S. V. Shiyanovskii, V. H. Bodnar, and O. D. Lavrentovich. Nematic polar anchoring strength measured by electric field techniques. *Journal of Applied Physics*, 86(8):4199–4213, 1999.

- [25] H. Yokoyama. Surface anchoring of nematic liquid crystals. *Molecular Crystals and Liquid Crystals*, 165(1):265–316, 1988.
- [26] R. F. de Souza, D.-K. Yang, E. K. Lenzi, L. R. Evangelista, and R. S. Zola. Effect of surface viscosity, anchoring energy, and cell gap on the response time of nematic liquid crystals. *Annals of Physics*, 346:14–21, 2014.
- [27] P. Oswald. Measurement with a rotating magnetic field of the surface viscosity of a nematic liquid crystal. *Europhysics Letters*, 100(2):26001, 2012.
- [28] P. Oswald, G. Poy, F. Vittoz, and V. Popa-Nita. Experimental relationship between surface and bulk rotational viscosities in nematic liquid crystals. *Liquid Crystals*, 40(6):734–744, 2013.
- [29] A. D. Rey. Periodic textures of nematic polymers and orientational slip. *Macromolecules*, 24(15):4450–4456, 1991.
- [30] G. E. Durand and E. G. Virga. Hydrodynamic model for surface nematic viscosity. *Physical Review E*, 59(4):4137–4142, 1999.
- [31] J. G. McIntosh and F. M. Leslie. Flow induced surface switching in a bistable nematic device. *Journal of Engineering Mathematics*, 37(1–3):129–142, 2000.
- [32] A. J. Davidson and N. J. Mottram. Flexoelectric switching in a bistable nematic device. *Physical Review E*, 65(5):051710, 2002.
- [33] G. Barbero and E. K. Lenzi. Importance of the surface viscosity on the relaxation of an imposed deformation in a nematic liquid crystal cell. *Physics Letters A*, 374(13–14):1565–1569, 2010.
- [34] R. T. de Souza, E. K. Lenzi, and L. R. Evangelista. Surface viscosity and reorientation process in an asymmetric nematic cell. *Liquid Crystals*, 37(12):1559–1568, 2010.
- [35] R. F. de Souza, E. K. Lenzi, R. T. de Souza, L. R. Evangelista, Q. Li, and R. S. Zola. Surface induced twist in nematic and chiral nematic liquid crystals: stick-slip-like and constrained motion. *Soft Matter*, 14(11):2084–2093, 2018.
- [36] M. Kléman and S. A. Pikin. A new kind of orientation instability in Couette flow nematics with finite anchoring energy. *Journal de Mécanique*, 18(4):661–672, 1979.
- [37] J. Quintans Carou, B. R. Duffy, N. J. Mottram, and S. K. Wilson. Steady flow of a nematic liquid crystal in a slowly varying channel. *Molecular Crystals and Liquid Crystals*, 438(1):237/[1801]–249/[1813], 2005.
- [38] J. Quintans Carou, B. R. Duffy, N. J. Mottram, and S. K. Wilson. Shear-driven and pressure-driven flow of a nematic liquid crystal in a slowly varying channel. *Physics of Fluids*, 18(2):027105, 2006.
- [39] A. Sengupta, U. Tkalec, M. Ravnik, J. M. Yeomans, C. Bahr, and S. Herminghaus. Liquid crystal microfluidics for tunable flow shaping. *Physical Review Letters*, 110(4):048303, 2013.
- [40] T. G. Anderson, E. Mema, L. Kondic, and L. J. Cummings. Transitions in Poiseuille flow of nematic liquid crystal. *International Journal of Non-Linear Mechanics*, 75:15–21, 2015.
- [41] M. Crespo, A. Majumdar, A. M. Ramos, and I. M. Griffiths. Solution landscapes in nematic microfluidics. *Physica D: Nonlinear Phenomena*, 351–352:1–13, 2017.
- [42] V. M. O. Batista, M. L. Blow, and M. M. Telo da Gama. The effect of anchoring on the nematic flow in channels. *Soft Matter*, 11(23):4674–4685, 2015.
- [43] H. Hong. In-Plane Switching (IPS) technology. In J. Chen, W. Cranton, and M. Fihn, editors, *Handbook of Visual Display Technology*, chapter 7.3.3, pages 1469–1483. Springer, 2012.
- [44] P. Raynes. Twisted Nematic and Supertwisted Nematic LCDs. In J. Chen, W. Cranton, and M. Fihn, editors, *Handbook of Visual Display Technology*, chapter 7.3.1, pages 1433–1444. Springer, 2012.
- [45] P. Pieranski and E. Guyon. Shear-flow-induced transition in nematics. *Solid State Communications*, 13(4):435 – 437, 1973.
- [46] I. Zúñiga and F. M. Leslie. Shear-flow instabilities in non-flow-aligning nematic liquid crystals. *Liquid Crystals*, 5(2):725–734, 1989.
- [47] D. J. Ternet, R. G. Larson, and L. G. Leal. Flow-aligning and tumbling in small-molecule liquid crystals: pure components and mixtures. *Rheologica Acta*, 38(3):183–197, 1999.

- [48] S. D. Hunnisett and J. C. A. van der Sluijs. Ultrasonic shear and capillary viscosity study of 4-cyano-4'-n-heptylbiphenyl in the nematic and the isotropic state. *Journal de Physique – Lettres*, 44(2):L-59–L-63, 1983.
- [49] A. G. Chimielewski. Viscosity coefficients of some nematic liquid crystals. *Molecular Crystals and Liquid Crystals*, 132(3–4):339–352, 1986.
- [50] M. T. Viciosa, A. M. Nunes, A. Fernandes, P. L. Almeida, M. H. Godinho, and M. D. Dionísio. Dielectric studies of the nematic mixture E7 on a hydroxypropylcellulose substrate. *Liquid Crystals*, 29(3):429–441, 2002.
- [51] Y. Hori. *Hydrodynamic Lubrication*. Springer, 2006.
- [52] MATLAB. *version 9.6.0.1114505 (R2019a)*. MathWorks, 2019.